TECHNISCHE
UNIVERSITÄT
WIEN
Vienna University of Technology

Diplomarbeit

Deformable hard particles confined in a disordered porous matrix

zur Erlangung des akademischen Grades
Diplom-Ingenieur
im Rahmen des Studiums
Technische Physik

eingereicht von
Alexander Stadik
Matrikelnummer 1326065

ausgeführt an der
Technischen Universität Wien
Fakultät für Physik

unter der Leitung von
Ao.Univ.Prof. DI Dr. Gerhard Kahl

. . . .
Unterschrift (Betreuer)

. . . .
Unterschrift (Student)

Wien, am December 15, 2019

Zusammenfassung

Kolloide sind im Alltag allgegenwärtig, einschließlich zahlreicher industriellen Anwendungen: beispielsweise als Dünger in der Agrikultur, oder im Bergbau zur Verbesserung des Ertrags bei der Treibstoffgewinnung. Aber ebenfalls im akademischen Bereich wächst das Interesse an der Erforschung von Kolloiden in den Bereichen der Physik, Chemie, Biologie und Medizin. Ein Teilgebiet dieser Forschung, welches besonders für den industriellen Sektor von Relevanz ist, ist die Untersuchung des Verhaltens von kolloidalen Teilchen eingebettet in ein poröses Medium; solch einen Fall findet mein beispielweise bei Proteinmolekülen im Cytoplasma der Zellen. Diese Möleküle sind allerdings nicht starr in ihrer Form (wie oft angenommen wird). Sie sind in der Lage sich zu verformen und können ihre Gestalt ihrer Umgebung anpassen. Diese Eigenschaft vereinfacht es ihnen sich durch ihre entsprechende Umgebung zu bewegen.

Das Ziel dieser Arbeit war es ein realistisches Model zu finden zur Erforschung solcher Systeme von deformierbaren, kolloidalen Teilchen eingebetten in eine ungeordnete poröse Matrix. Im Bestreben eines systematischen Vorgehens, untersucheten wir zuerst die statischen und dynamischen Eigenschaften von harten Teilchen, welche ihre ursprünglich kugelförmige Gestalt in eine ellipsoide verändern können. Darauffolgend betteten wir diese Teilchen in eine Matrix ein, bestehend aus starren (undeformierbaren) kugelförmigen Teilchen, wobei nur die erste Art von Teilchen die Möglichkeit besitzt sich zu bewegen. Wir untersuchten umfangreich wie sich dabei die Fähigkeit dieser Teilchen sich zu verformen auf ihre statischen und dynamischen Eigenschaften auswirkt. Dies führten wir im Rahmen zahlreicher entsprechend entwickelter Monte-Carlo Simulationen durch. Wie erwartet, konnten wir quantitativ verifizieren, dass eine erhöhte Fähigkeit sich zu verformen sich positiv auf das Bewegungsvermögen der Teilchen auswirkt, während sie sich durch die poröse Matrix bewegen.

Abstract

Colloids are ubiquituous in every day life, including many industrial applications: for instance, colloidal particles are used as fertilizers in agricultural applications or in mining industry for improving the yield in oil recovery processes. But also in the academic sector an increasing share of research has been dedicated during past years to colloids in the fields of physics, chemistry, biology or medicine. One subfield of research which is of particular relevance in industrial applications are studies of colloidal particles immersed into a disordered porous media; such a scenario is, for instance, encountered when proteins move through the cytoplasm of cells. These colloidal molecules are not rigid (as one often assumes), but deformable and can strongly adapt their shape according to the surrounding environment. This capacity enables these particles to propagate more easily through the related environment.

The goal of this thesis was to find and to investigate a realistic system of deformable colloidal particles confined in a disordered porous matrix. In an effort to proceed in a systematic manner, we have first examined the static and the dynamic properties of a system of hard particles which can deform their shape from a spherical one into an ellipsoidal one. Then we have immersed these particles into a matrix, formed by rigid (i.e., undeformable) spherical particles, where the former ones represent the mobile component. We have investigated in detail how the capacity of deformation influences the static and the dynamic properties of the mobile particles. Investigations were carried out on large scales with suitably developed Monte Carlo simulations. As expected, we could verify on a quantitative level that an increased deformability enhances the mobility of the deformable particles as they move through the matrix.

Contents

CHAPTER 1

Introduction

In this first chapter we want to convey to the reader the motivation for writing this thesis and also give a physical background underlying it. Over the course of this work we will primarily give analysis of data from simulations and calculations of these. They will represent the static structure and dynamical behavior of the presented models, and are therefore critical for a legitimate examination of such a model. But nonetheless this procedure can sometimes lack connections to real physical phenomena, further completing the picture of a model. Therefore, through this chapter we want to give to the reader the opportunity, to gain these pictures, related to the models we want to discuss. We hope that the reader can recover them to gain a deeper understanding. However this chapter will only provide an overall picture of the main physical backgrounds. Every chapter will also contain another small introduction extending these pictures specifically for their topics.

1.1 Colloids

The first concept we want to introduce in this preface is the "colloid". The name was first used by Thomas Graham a Scottish chemist in 1891. He studied the diffusion of substances through semi-permeable membranes. Hence, he defined colloids as exactly these substances that cannot diffuse through membranes. Over his research he mainly studied materials such as starch, dextrose or caramel etc.. Since he associated these materials mainly through their organic nature he named them after the Greek words $\kappa \acute{o} \lambda \lambda \alpha$ (kólla - glue) and $\varepsilon \acute{\iota} \delta o \varsigma$ (eídos - kinds) - the *sticky ones.*

Today there exist many modern definitions of *colloids*, satisfying their real nature. The main feature over which colloids are frequently defined, is that one does not need to know the exact atomic or molecular configuration of these particles, to understand their physical behavior. They are of sufficient size, so that quantum effects can be neglected and can therefore be studied on a coarse grained level. But particles which get the label *colloids* still have to be small enough to retain a stable mixture as a collective substance. This means that real colloids exist within the "mesoscopic" regime - 1μm to 1nm. Most modern definitions of a colloidal system contain a second feature; such a system needs to be a mixture of two substances, one which is a solvent or "dispersed medium", the other one consisting of bigger particles which are immersed in the solvent. These different kind of definitions still lead to further confusion, as frequently only the second type of particles of this mixture carry the label colloid, even when talking about a colloidal system.

1.2 Flexibility of particles

Through the example of a protein we want to introduce another important concept of this work. In the previous definition we claimed that it is not required to know the atomic or molecular structure of colloids, to make predictions about their behavior. But in reality for instance proteins consist of complex atomic structures where the pieces they consist of will move and dislocate from their position to some extent. They exist in a great variety of forms and structures and are not completely rigid. Proteins can deform and will adapt to their environment accordingly. This would suggest an important role of their form or of the atomic structure to completely understand their exact behavior. For example enzymes can adjust their shape to fit around a ligand they move through or in general spherical particles can fit through holes which are much narrower than their diameter would allow by deforming themselves.

Particles which show these traits are therefore called *flexible* particles. The reason for the ability of particles to deform is often closely connected to their biological function, which makes it necessary to understand their *deformability* to grasp those very functions. While real proteins have complex shapes, nonetheless, many types have an overall spherical form, or at least it serves as a sufficient approximation. Further even though they consist of smaller parts most retain a somewhat compact structure.

To summarize: while one needs to know the atomic structure of a protein in order to understand its biological function, its physical properties as a single particles can be understood without this knowledge. However to get a complete picture one needs to take into account both views.

These two definitions - the *collloid* and *deformability* of particles - represent the main background of this thesis. Every concept presented over the course of this work will revolve around them. Consequently the theoretical models we want to present also revolve around even these concepts. Therefore we structured this work into a first part giving the mathematical foundation of the models, and three major parts revolving around their respective models:

- **(i)** Initially we will give details of the simulation techniques used in all models and give a short overview of the mathematics behind all post-processing tools we will use.
- **(ii)** As a first major part we will thoroughly discuss a model containing deformability; the deformable-hard-spheroid model (DHS model). We will examine changes that deformability introduces into a system compared to one consisting solely of rigid particles. We will look especially at the static structure, dynamic behavior and phase transitions which may arise therefrom.
- **(iii)** The second major part will revolve around rigid particles in a porous environment and how to generate such systems. For that we will present the hard-sphere-quenched-annealed model (HS-QA model) and we will look in detail at different

manifestations of such systems.

(iv) The third and last part will combine the previous two concepts and models into the deformable-hard-spheroid-quenched-annealed model (DHS-QA model). In the corresponding chapter we will give a rigorous view over all capabilities that flexible particles gain in porous confinement and which phenomenons arise.

There are many additional definitions and methods that the reader needs to know, like for example the conventional concepts to define and predict the static structure of a system or the dynamic behavior of particles. These concepts will be presented in the very chapter they are used and needed, to create a fixed line which the reader can follow throughout the thesis. Through this structure we try to set up an environment where the reader can gain a natural feeling for the concepts.

CHAPTER 2

Deformable hard sphere model

The goal of this chapter is to study the effects of deformability of originally spherical particles on the static and dynamic properties. To gain this information in the most simple and computationally efficient way, we use the model of deformable hard spheres (DHS) put forward by Batista and Miller [2]. This model will be explained in the following.

The basis of the deformable sphere model is the hard ellipsoid of revolution (HER) model. Particles are described as hard spheres of revolution (spheroids) with equation $\frac{x^2+y^2}{a^2} + \frac{z^2}{c^2} = 1$. HER's are ellipsoids where two of the semi-axes have the same length $a = b \neq c$, producing thus a surface of revolution. Its rotational symmetry is set to the z-axis for the purpose of simplicity.
The potential used in the HER model is the pair potential of two hard spheroids, with their center separated by a vector $\mathbf{r}$ and orientations $\boldsymbol{\Omega_1}$ and $\boldsymbol{\Omega_2}$.

$$V(\mathbf{r}, \Omega_1, \Omega_2) = \begin{cases} 0 & \text{if the partciles overlap} \\ \infty & \text{if the particly do not overlap} \end{cases} \tag{2.1}$$

Since the detection of overlaps for impenetrable spheroidal particles is not as simple as in the case of hard spheres, an efficient algorithm for its detection is necessary. A practical method will be discussed in the first section of the next chapter.

In the DHS model a particle is taken originally as a sphere with diameter σ and volume $V = \frac{\pi\sigma^3}{6}$. Within the model it is then possible for the particles to change their form into a spheroid of revolution through elongation. During this deformation the axes lengths have to fulfill conditions to ensure preservation of the particle volume, thus

$$a = \frac{\sigma}{2} x^{\frac{1}{3}} \tag{2.2}$$

$$c = \frac{\sigma}{2} x^{-\frac{2}{3}} \tag{2.3}$$

introducing the aspect ratio $x = a/c$. Therefore it is convenient to quantify the distortion of the spheres by x. x represents the only additional degree of freedom for the particles in the DHS model, which is the main trait for its simplicity. In particular for an aspect ratio of $x < 1$ the colloids take on a oblate form, for $x > 1$ a prolate form and for $x = 1$ the spherical (see Fig. 2.1).

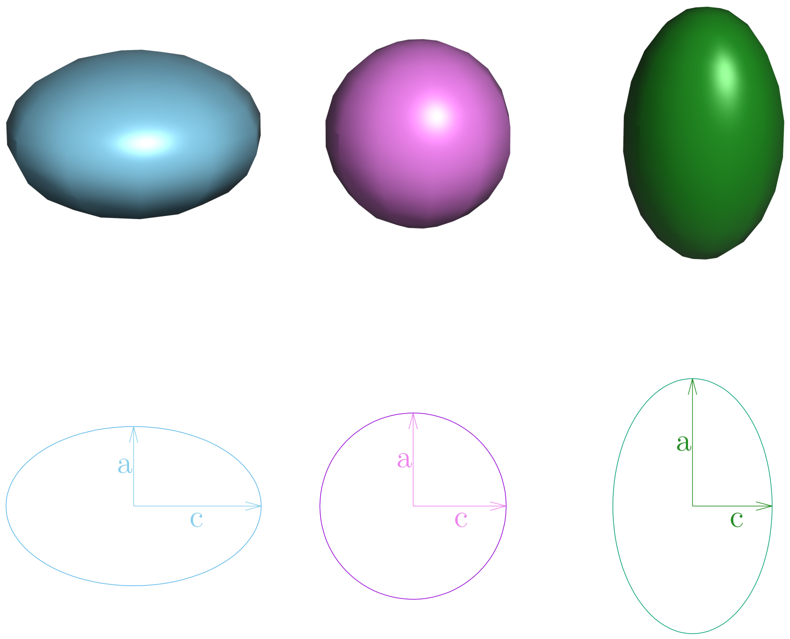

Figure 2.1: Shapes of deformed spheroids of revolution (left $x < 1$ and right $x > 1$) originating from a sphere (center $x = 1$) with aspect ratio $x = a/c$ (see Eqs. (2.2), (2.3))

We emphasize that these particles are described as deformable but incompressible spheroids, while for real colloids is also possible to be compressible. However, our model enables us to observe the influence of deformability decoupled from changes in the packing fraction of the simulated system, which is not the case anymore when introducing compressibility. Further real colloids can undergo more complex deformations than elongation and can also deviate from a spherical form, which makes the DHS-model something like a first-order approximation. However in most cases elongation is the first shape deformation that becomes important for colloids. [1] For a system consisting of HS particles, since it is an athermal model, the only relevant control parameters are the particle diameter σ and the number density $\rho = N/V_{\text{sys}}$. With N the number of particles and V_{sys} the volume of the system. Commonly these two parameters are combined into the dimensionless packing fraction of the system

$$\phi = \frac{NV}{V_{\text{sys}}} = \frac{\pi}{6}\rho\sigma^3. \tag{2.4}$$

Thus ϕ becomes the only relevant parameter to the thermodynamics of a HS-system. Since in the DHS-model the volume of the particles V is preserved during deformation, we can maintain ϕ as a control parameter.

The extent to which the particles deform in the DHS model is controlled by an energy penalty. Batista and Miller [2] chose the form of the energy function of deformation they used, with a liquid droplet in mind. The work required to deform a droplet of fixed volume from its spherical form is proportional to its surface tension γ and the increase

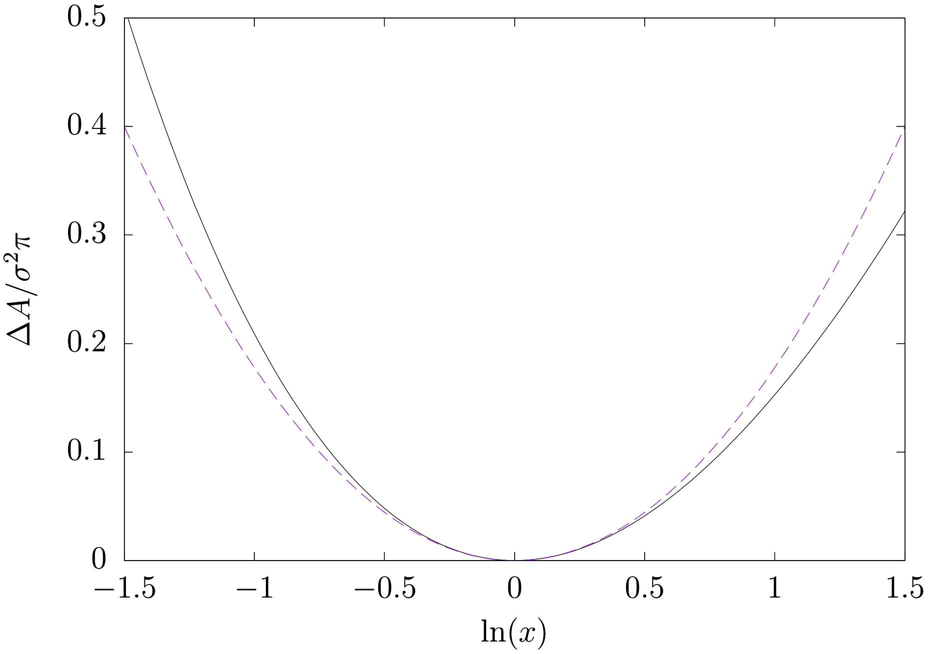

Figure 2.2: Solid line: increase of surface area of a spheroid (ΔA) relative to a sphere of the same volume, as a function of $\ln(x)$, x being the aspect ratio of the spheroid. Dashed line: approximation of ΔA up to second order in $\ln(x)$.

in surface area ΔA compared to a sphere,

$$\Delta A = 2\pi a^2 + \frac{\pi c^2}{d} \ln\left(\frac{1+d}{1-d}\right) - 4\pi(\frac{\sigma}{2})^2, \tag{2.5}$$

where the ellipticity d is defined, in case of a oblate spheroid, as

$$d = \sqrt{1 - \frac{a^2}{c^2}} = \sqrt{1 - x^2}, \tag{2.6}$$

and in case of a prolate spheroid, as

$$d = \sqrt{1 - \frac{c^2}{a^2}} = \sqrt{1 - \frac{1}{x^2}}. \tag{2.7}$$

ΔA is a complicated function of x. However, visible in Fig. 2.2 it can be approximated in a symmetric form around $x = 1$, then considered as a function of $\ln(x)$. Therefore the change in surface area ΔA will be expanded around $\ln(x) = 0$ in a Taylor series up to second order:

$$\frac{\Delta A}{\sigma^2\pi} \approx \frac{8}{45}\ln(x)^2 + \mathcal{O}(\ln(x)^3) \tag{2.8}$$

Related to ΔA is a change in energy $U = \gamma\Delta A$, with the surface tension of a liquid droplet γ. By using Eq. (2.8) U can be expressed through

$$U(x) = \kappa \ln(x)^2. \tag{2.9}$$

Equation (2.9) indicates a harmonic dependency on $\ln(x)$ with the spring constant κ. This constant, the stiffness parameter κ, is related to γ via

$$\kappa = \frac{1}{2}(\Delta A)''\gamma = \frac{8}{45}\sigma^2\pi\gamma. \tag{2.10}$$

$(\Delta A)''$ denotes the second derivate of the increase in surface area as a function of $\ln(x)$. In the limit $\lim \kappa \to \infty$ deformation is suppressed and one gets a simply hard sphere model. In case of finite κ the shape of the particles undergoes thermal fluctuations which depend on the linked parameter $\beta\kappa$ where $\beta^{-1} = k_B T$ denotes the thermal energy. Finally the total potential energy of a system consisting of deformable spheres is

$$U_{\text{tot}} = \sum_{i<j} V(\mathbf{r}, \Omega_i, \Omega_j) + \sum_i U(x_i) \tag{2.11}$$

where V is the is the hard spheroid potential (see Eq. (2.1)).

Since compared to the HS-model the DHS-model is not athermal anymore, we gain another control parameter to the thermodynamics of a system based on the DHS-model. A convenient parameter is $\beta\kappa$, which, since it will occur without exception in this paired form, from this point on will inherit the name of κ *stiffness*. When talking about the ability to deform itself we will use the term *deformability*.

CHAPTER 3

Methods

This chapter gives an overview over the methods and algorithms used throughout this thesis. First we will provide a general description of the simulation method we use with its individual steps for simulating the motion and the shape deformation of our particles. Next we will introduce a criterion to detect overlaps between the different possible shapes of the particles. At last we will define some mathematical tools for analyzing the static and dynamic properties of the simulated system of the DHS-model.

3.1 Simulation method

Throughout this thesis constant-NVT Monte Carlo simulations were performed. To reach the necessary variety of packing fractions different particle diameters σ where used, while all results will be presented in a way not depending on σ to allow comparability. Depending on the packing fraction, different numbers of particles were used, reaching from $N = 432$ to 3500, to enable an appropriate statistical evaluation. As the simulation cell a unit cube with $V_{\text{sys}} = 1$ was used, where periodic boundary conditions where applied on all six sides.

A particle is characterized by its position $\mathbf{r} = (r^1, r^2, r^3)$, its orientation, expressed via the Euler-angles $(\varphi, \vartheta, \psi)$, and its aspect ratio x the ratio between the major and the minor axis of the ellipsoid. (see Eqs. (2.2), (2.3))

A simulation consists of a number of sweeps, where again one sweep consists of N trial translational moves, N rotational moves and N attempted shape deformations. These "moves" shall be further explained in the following.

3.1.1 Translational moves

Translational moves are made by randomly choosing a particle and creating an arbitrary displacement. This happens by shifting its coordinates (r^1, r^2, r^3) by a spatial value

$\in [-\Delta r_{\max}/2, \Delta r_{\max}/2]$ by using a uniformly distributed random number $rand() \in [0,1]$

$$\begin{aligned} r^1_{\text{new}} &= r^1 + \Delta r_{\max}(0.5 - rand()) \\ r^2_{\text{new}} &= r^2 + \Delta r_{\max}(0.5 - rand()) \\ r^3_{\text{new}} &= r^3 + \Delta r_{\max}(0.5 - rand()). \end{aligned} \tag{3.1}$$

If the new coordinates do not generate an overlap with another particle the move is accepted, otherwise rejected. The parameter Δr_{max} is changed dynamically during the simulation to guarantee an acceptance rate of the translational moves of about 50 percent.

3.1.2 Rotational moves

Since the simulated particles are in general non-spherical, it is also necessary to implement rotational moves. During the simulation only the Euler-angles $(\varphi, \vartheta, \psi)$ of each particle are stored. The orientation of the principal axis of a particle, $\mathbf{a}$, can be calculated when needed via the matrix $\mathcal{S} = \mathcal{S}(\varphi, \vartheta, \psi)$ which is a product of the conventional rotation matrices:

$$\mathcal{S} = \begin{pmatrix} \cos\psi & \sin\psi & 0 \\ -\sin\psi & \cos\psi & 0 \\ 0 & 0 & 1 \end{pmatrix} \begin{pmatrix} 1 & 0 & 0 \\ 0 & \cos\vartheta & \sin\vartheta \\ 0 & -\sin\vartheta & \cos\vartheta \end{pmatrix} \begin{pmatrix} \cos\varphi & \sin\varphi & 0 \\ -\sin\varphi & \cos\varphi & 0 \\ 0 & 0 & 1 \end{pmatrix} \tag{3.2}$$

The matrix given in Eq. (3.2) is applied to the unit vectors $\mathbf{e}_i$ to obtain the corresponding three principal axes $\mathbf{a}_i$ of the particle

$$\mathbf{a}_i = \mathcal{S}\mathbf{e}_i. \tag{3.3}$$

Therefore for a trial rotation of a particle the Euler-angles of a randomly chosen particle are changed about an angle $\in [-\Delta\varrho_{\max}/2, \Delta\varrho_{\max}/2]$.

$$\begin{aligned} \varphi_{\text{new}} &= \varphi + \Delta\varrho_{\max}(0.5 - rand()) \\ \vartheta_{\text{new}} &= \vartheta + \Delta\varrho_{\max}(0.5 - rand()) \\ \psi_{\text{new}} &= \psi + \Delta\varrho_{\max}(0.5 - rand()), \end{aligned} \tag{3.4}$$

generating a new orientation. Again, the move is accepted if no overlap is created for the new orientation, otherwise it is discarded. Also $\Delta\varrho_{\max}$ is dynamically changed during the simulation to ensure a acceptance rate of the moves of about 50 percent.

3.1.3 Shape deformation

In chapter 2 the initial model this thesis is based on was presented and discussed. The model allows to introduce deformability of the particles into the system via elongation. The potential which controls the energy penalty for deformation is a function of $\ln(x)$ (see Eq. (2.9)), x being the aspect ratio of the spheroid. Therefore we apply a displacement in shape by adding an arbitrary change to $\ln(x) \in [-\Delta L_{\text{max}}/2, \Delta L_{\text{max}}/2]$.

$$\ln(x)_{\text{new}} = \ln(x) + \Delta L_{\text{max}}(0.5 - rand()) \tag{3.5}$$

where ΔL_{max} is changed during the simulation to ensure an acceptance rate of the deformations of about 50 percent. Like in the case of translational or rotational displacement a trial change in elongation is only accepted if it does not create an overlap with another particle.
But additionally shape deformation is related to an energy penalty (see Eq. (2.9)) which is implemented in the simulation using a Metropolis algorithm, with the acceptance rate

$$p = \min\left(1, \exp(-\beta\Delta U)\right) = \min\left(1, \exp(-\beta\kappa(\ln(x_{\text{new}})^2 - \ln(x_{\text{old}})^2)\right). \tag{3.6}$$

An arbitrary number $rand() \in [0,1)$ is generated and compared to p, if $rand() < p$ the deformation is accepted, otherwise discarded.

The parameter $\beta\kappa$, where $\beta^{-1} = k_{\text{B}}T$ (k_{B} being the Boltzmann constant and T the temperature of the system), is used to control the deformability of the particles. This induces ”thermal fluctuations” of the particle shape into the simulations. Beside these natural fluctuations, the final shape of an individual after one sweep will only depend next to the packing fraction of the system ϕ, on the overlap criterion specified in the following.

3.2 Overlap criterion and contact function

Like already mentioned in the last chapter, detecting overlaps of ellipsoidal particles is not as easy as in case of spherical particles, where comparing the inter-particle distance with their diameter σ is sufficient. A considerably more complex method has to be used, which has to take into account the orientations of the principal axes of the particles, in addition to the distance of the centers of the particles. An efficient and reliable method which fulfills these traits was devised by Perram and Wertheim [5].

In this method first a function is required that expresses the orientation of a single particle in space. It has to be non-negative and has to satisfy the conditions

$$F_A(\mathbf{r} - \mathbf{r}_A, \Omega_A) \begin{cases} < 1 \text{ if } \mathbf{r} \text{ inside A} \\ = 1 \text{ if } \mathbf{r} \text{ on the surface of A} \\ > 1 \text{ if } \mathbf{r} \text{ outside A} \end{cases} \tag{3.7}$$

with $\Omega = (\varphi, \vartheta, \psi)$. Perram and Wertheim give a simple solution in the form of

$$F_A(\mathbf{r} - \mathbf{r}_A, \Omega_A) = (\mathbf{r} - \mathbf{r}_A)^T \mathcal{A}^{-1}(\mathbf{r} - \mathbf{r}_A) \tag{3.8}$$

where an symmetric and positive definite matrix $\mathcal{A}$ was used

$$\mathcal{A}(\Omega_A) = \sum_{i=1}^{3} \mathcal{S}(\Omega_A)\, \mathbf{e}_i \mathbf{e}_i^T \mathcal{S}^T(\Omega_A) h_i^2 \tag{3.9}$$

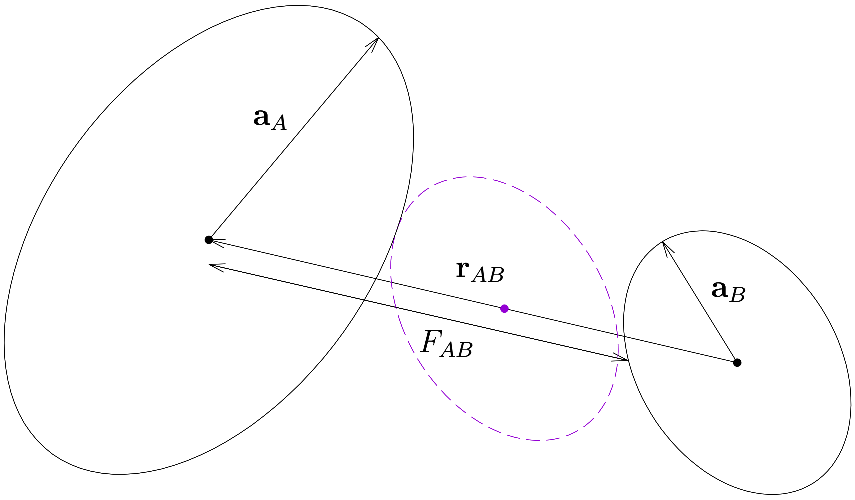

Figure 3.1: Visualization of the contact function. $\mathbf{a}_A$ and $\mathbf{a}_B$ are the main principal axes of particle A and B respectively. $\mathbf{r}_{AB}$ is the distance between the centers of particle A and B. F_{AB} visualizes the value of the contact function for $\mathbf{r}_{AB}$.

with the matrix $\mathcal{S}(\Omega_A)$ as in (3.2). Here $\mathbf{e}_i$ again denote the unit vector and h_i the length of the respective semi-axis.

In order to get an adequate contact function Perram and Wertheim [5] define the function

$$F(\mathbf{r}, \lambda; \mathbf{r}_A, \mathbf{r}_B, \Omega_A, \Omega_B) = F(\mathbf{r}, \lambda) = \lambda F_A(\mathbf{r} - \mathbf{r}_A, \Omega_A) + (1 - \lambda) F_B(\mathbf{r} - \mathbf{r}_B, \Omega_B) \tag{3.10}$$

which depends on the positions $\mathbf{r}_A, \mathbf{r}_B$ and the orientations Ω_A, Ω_B of two different ellipsoids A and B, and on the arbitrary vector $\mathbf{r}$.
For a fixed $\lambda \in [0, 1]$ the function $F(\mathbf{r}, \lambda)$ has a unique minimum at $\mathbf{r} = \mathbf{r}(\lambda)$, for $\lambda = 0$ it occurs at $\mathbf{r} = \mathbf{r}_B$ with $F(\mathbf{r}_B, 0) = 0$ and for $\lambda = 1$ at $\mathbf{r} = \mathbf{r}_A$ with $F(\mathbf{r}_A, 0) = 0$. Otherwise, $F(\mathbf{r}(\lambda), \lambda)$ can be shown to be concave. $F(\mathbf{r}(\lambda), \lambda)$ can be minimized by solving $\nabla F = 0$, which gives the equation

$$\lambda \mathcal{A}^{-1}(\mathbf{r} - \mathbf{r}_A) + (1 - \lambda)\mathcal{B}^{-1}(\mathbf{r} - \mathbf{r}_B) = 0, \tag{3.11}$$

using $\mathbf{r}_{AB} = \mathbf{r}_A - \mathbf{r}_B$ and the matrix

$$\mathcal{C} = [\lambda \mathcal{B} + (1 - \lambda)\mathcal{A}]^{-1}. \tag{3.12}$$

The solution $\mathbf{r}(\lambda)$ of Eq. (3.11) can be expressed conveniently in two forms:

$$\begin{aligned} \mathbf{r}(\lambda) - \mathbf{r}_A &= (1 - \lambda)\mathcal{A}\mathcal{C}\mathbf{r}_{AB} \text{ or} \\ \mathbf{r}(\lambda) - \mathbf{r}_B &= -\lambda \mathcal{B}\mathcal{C}\mathbf{r}_{AB}, \end{aligned} \tag{3.13}$$

which enabled Perram and Wertheim to rewrite the function in Eq. (3.10) in a form which does not contain $\mathbf{r}(\lambda)$ explicitly

$$F[\mathbf{r}(\lambda), \lambda] = \lambda(1-\lambda)\mathbf{r}_{AB}^{T}\mathcal{C}\mathbf{r}_{AB}. \tag{3.14}$$

Maximization of this equation in λ gives the desired contact function

$$F(\mathbf{r}_{AB}, \Omega_A, \Omega_B) = \max_{0\leq\lambda\leq 1} \lambda(1-\lambda)\mathbf{r}_{AB}^{T}\mathcal{C}\mathbf{r}_{AB} \begin{cases} < 1 \text{ for A and B overlapping} \\ = 1 \text{ for A and B tangent} \\ > 1 \text{ for A and B non-overlapping} \end{cases} \tag{3.15}$$

Perram and Wertheim also gave a geometric interpretation to their contact function. By scaling the size of each of the ellipsoids ($i = A, B$) by a non-negative linear factor $\tilde{h}_i$ they interpret the path $\mathbf{r}(\lambda)$ as the locus of points where these scaled ellipsoids externally touch each other. The function given in Eq. (3.10) assumes the respective value of the scaling factor, i.e.

$$F_A[\mathbf{r}(\lambda), \lambda] = \tilde{h}_A^2, \quad F_B[\mathbf{r}(\lambda), \lambda] = \tilde{h}_B^2. \tag{3.16}$$

Consequently the maximum of that defines the unique point on the path $\mathbf{r}(\lambda)$ where the scaling factors are equal $\tilde{h}_A = \tilde{h}_B = \tilde{h}$ and thus the contact function of Eq. (3.16) $F(\mathbf{r}_{AB}, \Omega_A, \Omega_B) = \tilde{h}^2$. If the necessary scaling factor is smaller than 1 the particles have to be downsized, hence, they overlap. Otherwise if it is equal to 1 the particles touch exactly.

3.3 Correlation functions

After investigating the system using a convenient simulation technique, one also needs the appropriate tools for analyzing its properties and to identify the influence of certain variables of the model as compared to a reference model. Additionally, some of these evaluations can be compared and falsified through experiments that are viable in principal. Some of these analysis tools will be introduced in this section.

We will divide the necessary functions into two categories:

(i) ones that give information about the *static* structure of the system

(ii) and others that determine *dynamical* properties.

In this thesis, to understand the static structure, we explicitly calculate the pair-correlation function, the static structure factor, the distribution of aspect-ratio of the ellipsoids and the correlation function of the orientation of the particles as a function of the pair correlation.

To access the dynamical properties of the system we calculate the mean squared displacement, its logarithmic derivate and the intermediate scattering function.

In this chapter only a mathematical view of the post-processing tools will be given that leads to these functions. Over the later chapters also a more practical approach will be taken, where we will discuss and interpret the typical important aspects of these function, through simulation results.

3.3.1 Pair-correlation function

First we will introduce the pair-correlation function (also radial distribution function RDF). It measures how the density varies while increasing the distance from a reference particle. Introducing $n(r)$ as the number of particles located in the shell $[r, r+\delta r]$ around the central particle the radial distribution can be calculated with [8]

$$g(r) = \frac{n(r)}{\Delta V \rho} \tag{3.17}$$

where $\Delta V = \frac{4\pi}{3}((r+\Delta r)^3 - r^3)$ is the volume of the above spherical shell. ρ is the overall number density of the system which in our case simply is $\rho = \frac{N}{V_{\text{sys}}} = N$. Since our system is limited by the simulation box we can calculate $n(r)$ by simply binning the particle separations in a histogram.

$$g(r) = \frac{1}{N}\left\langle \frac{1}{\Delta V} \sum_{i \neq j}^{N}\sum \delta(r - r_{ij}) \right\rangle \tag{3.18}$$

where $r_{ij} = |\mathbf{r}_i - \mathbf{r}_j|$ is the absolute value of the inter-particle distance.
$g(r)$ gives information about "preferred" distances particles tend to position themselves in a specific system. Due to the deformation introduced in the DHS-model the particles gain another degree of freedom, their orientation in relation to the reference frame of the system. Thus to get insight into the pair-wise orientation of the particles of a system Eq. (3.18) has to be extended to

$$g(r,\theta) = \frac{1}{N}\left\langle \frac{1}{\Delta V} \sum_{i \neq j}^{N}\sum \delta(r - r_{ij}) \frac{\delta(\theta - \theta_{ij})}{|\sin\theta_{ij}|} \right\rangle, \tag{3.19}$$

where the pair-wise orientation θ_{ij} is used defined by

$$\cos\theta_{ij} = \frac{\mathbf{a}_i^T \mathbf{a}_j}{|\mathbf{a}_i|\,|\mathbf{a}_j|}. \tag{3.20}$$

The vectors $\mathbf{a}_i$ and $\mathbf{a}_j$ denote the main principal axis of the particles i and j respectively (see Eq. (3.3)).

3.3.2 Static structure factor

Another tool characterizing the structure of the system is the static structure factor (SSF) $S(\mathbf{k})$ with $\mathbf{k}$ the scattering vector. It describes how material scatters incidental radiation. It therefore enables to interpret scattering patterns.

By calculating the static structure factor spatial correlations in reciprocal space are measured. To obtain it we start from the Fourier transform of the one-particle density.

$$\rho_{\mathbf{k}} = \sum_{i=1}^{N} e^{i\mathbf{k}\mathbf{r}_i}. \tag{3.21}$$

By multiplying this quantity with its complex conjugating and taking the ensemble average $\langle \cdot \rangle$ we get the standard expression for the static structure factor

$$\begin{aligned} S(\mathbf{k}) &= \frac{1}{N}\langle \rho_{\mathbf{k}}\rho_{-\mathbf{k}} \rangle \\ &= \frac{1}{N}\left\langle \sum_{i=1}^{N}\sum_{j=1}^{N} e^{i\mathbf{k}(\mathbf{r}_i-\mathbf{r}_j)} \right\rangle. \end{aligned} \tag{3.22}$$

Liquids and amorphous materials can be considered isotropic beyond nearest- neighbor distances [8]. In this case the scattering function only depends on the absolute magnitude of the scattering vector $k = |\mathbf{k}|$. Hence, a transfer between real and reciprocal space can be calculated by using a one-dimensional Fourier transform. By separating the diagonal terms (i.e. $i = j$) in Eq. (3.22) one obtains with Eq. (3.18) the static scattering function in the form of

$$S(k) = 1 + \frac{4\pi\rho}{k} \int_0^\infty r[g(r) - 1] \sin(kr) \mathrm{d}r. \tag{3.23}$$

This formula gives us a tool for a fast calculation of the scattering function. The integral extends over all particle separations and is evaluated by discrete integration. Since $g(r)$ converges fast to 1 for liquids it is sufficient to limit the integration by half of the box length [8].

3.3.3 Mean squared displacement

A quantity to characterize a system in its dynamical properties is the mean squared displacement (MSD). It measures the average ability of a particle to move through its environmental medium. The MSD is defined as

$$\delta r^2(t) = \frac{1}{N}\left\langle \sum_{i=1}^{N} |\mathbf{r}_i(t) - \mathbf{r}_i(0)| \right\rangle \tag{3.24}$$

where $\mathbf{r}_i(t)$ and $\mathbf{r}_i(0)$ denote the position of the particle $i \in [0, N]$ in the simulation box at a time t and at the time-origin $t = 0$ in time, respectively.

During this thesis we performed Monte-Carlo simulations, which in contrast to molecular dynamics simulations do not have a real time evolution, therefore we identify the sweeps as time steps. Additionally we have to modify Eq. (3.24) to include the drift of the center of mass of the simulation box [2]

$$\delta r^2(t) = \frac{1}{N}\left\langle \sum_{i=1}^{N} \left| \Big(\mathbf{r}_i(t) - \mathbf{r}_{cm}(t)\Big) - \Big(\mathbf{r}_i(0) - \mathbf{r}_{cm}(0)\Big) \right|^2 \right\rangle. \tag{3.25}$$

Here $\mathbf{r}_{cm}(t)$ and $\mathbf{r}_{cm}(0)$ are the position of the center of mass at the time t and $t = 0$.

The Einstein-Smoluchowski-relation connects the diffusion of particles in a system with the MSD of the particles by considering the diffusivity as a long-time-limit of the MSD. The diffusivity is a characteristic coefficient, which measures the ability of particles to propagate through their environment

$$D = \lim_{t \to \infty} \frac{\delta r^2(t)}{6t}. \tag{3.26}$$

In realistic systems the MSD might not follow the relation (3.26), but might rather fulfill the more universal law $\delta r^2(t) \propto t^z$. Thus it is more convenient to define an effective exponent z via the logarithmic derivate

$$z(t) = \frac{d[\log \delta r^2(t)]}{d[\log t]} \tag{3.27}$$

in order to identify and quantify these features at different regimes. If $z(t) > 1$ the behavior is denoted as super-diffusive, while if $z(t) < 1$ we call it sub-diffusive. Normal diffusion corresponds to regimes with $z(t) = 1$ and dynamic arrest to $z(t) = 0$.

3.3.4 Self intermediate scattering function

Another tool for characterizing the dynamical behavior of our systems is the self intermediate scattering function (ISF) $F_s(\mathbf{k}, t)$. This dynamic structure factor relates both spatial as time correlations. This function can be calculated via the correlations of the Fourier transform of the time dependent single-particle density [3]

$$\begin{aligned} F_s(k,t) &= \frac{1}{N} \langle \rho_k(t) \rho_{-k}(0) \rangle \\ &= \frac{1}{N} \left\langle \sum_{i=1}^{N} \sum_{j=1}^{N} e^{i\mathbf{k}\left(\mathbf{r}_i(t) - \mathbf{r}_j(0)\right)} \right\rangle. \end{aligned} \tag{3.28}$$

Again, since we use Monte-Carlo algorithm throughout this thesis, the motion of the center of mass has to be taken into account. Therefore 3.28 has to be modified.

$$F_s(k,t) = \frac{1}{N} \left\langle \sum_{i=1}^{N} \sum_{j=1}^{N} e^{i\mathbf{k}\left|\left(\mathbf{r}_i(t) - \mathbf{r}_j(0)\right) - \left(\mathbf{r}_{cm}(t) - \mathbf{r}_{cm}(0)\right)\right|} \right\rangle \tag{3.29}$$

The ISF encodes information about how the density correlations given by $S(k)$ (Eq. (3.23)) change as time progresses. It quantifies the structural relaxation of the material and therefore gives another view of its dynamical behavior. [7]

CHAPTER 4

Fluid phase

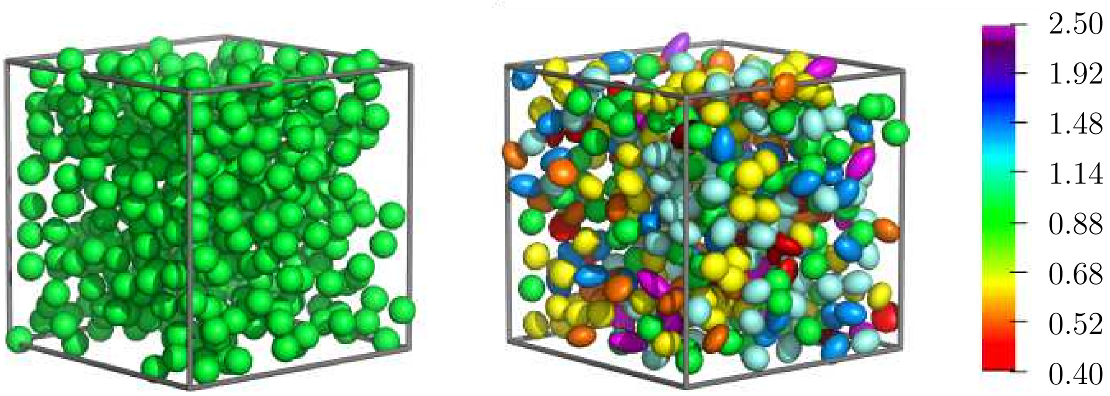

(a) Spheres

(b) Spheroids

Figure 4.1: Two snapshots of a system in its fluid phase at a packing fraction of $\phi = 0.226$ (a) - rigid spheres (i.e. $\beta\kappa = \infty$) and (b) - deformable spheres (with $\beta\kappa = 5$). In the latter case the particles are colored according to their aspect ratio, red for highly oblate, green for spherical, violet for highly prolate form, covering all the colors of the rainbow.

In the following chapters results of simulations of systems consisting of deformable spheres are presented. All were generated by using the simulation method and the analysis tools introduced in Chapter 3. In this chapter all systems considered will be in the fluid phase. General behavior of the spheroids and the correlation functions will be discussed, first their static structure and afterwards also their dynamical properties.

All simulations were performed with a constant-NVT Monte Carlo algorithm. The simulation box is fixed at a volume of $V_{\text{sys}} = 1$ and the number of particles in the system is $N = 432$. The packing fraction is controlled by increasing or decreasing the particle diameter of initially spherical particles.
To show an adequate picture of the influence of the two control parameters state points we examine are located on two paths in the parameter space of the DHS-model. For every result shown $\beta\kappa = \infty$ denotes undeformable hard spheres.

Path I: Stiffness parameter $\beta\kappa$ is fixed, while the packing fractions vary within $\phi \in [0.116; 0.502]$.

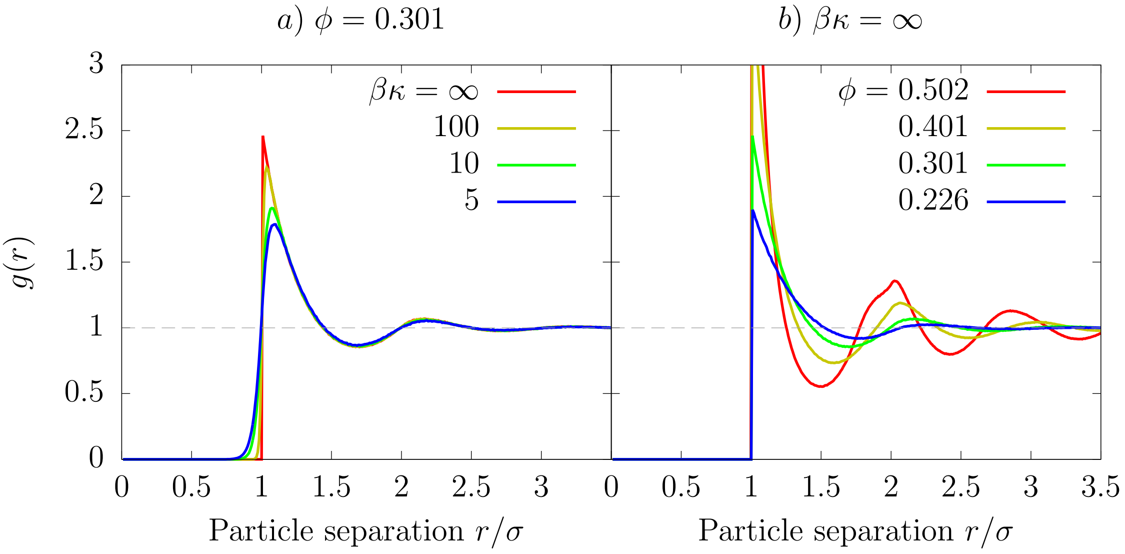

Figure 4.2: Pair correlation function $g(r)$ of a liquid system of deformable hard spheres as a function of r in units of σ.
Panel *a* for a selected packing fraction of $\phi = 0.301$, considering different values of $\beta\kappa$ (as labeled). Panel *b* results for fixed $\beta\kappa = \infty$, for different packing fractions (as labeled)

Path II: Stiffness parameters vary within $\beta\kappa \in [5, 10, 100, \infty]$, while the packing fraction ϕ is fixed.

4.1 Static structure

For the analysis of the static structure of the fluid phase of the DHS-model, as a first step we investigate the radial distribution function $g(r)$ (pair correlation function) given in Eq. (3.18).
In Figure 4.2 we present results for $g(r)$ for various combinations of the parameter ϕ or $\beta\kappa$. For reasons of completeness we displayed $g(r)$ for the limit of hard spheres ($\beta\kappa = \infty$) separately for selected packing fractions in the Panel *b* of Fig. 4.2. At $r = \sigma$ we observe the well-known sharp drop in $g(r)$, which originates from the fact that the closest distance of two spherical HS-particles is the diameter of the particle itself. We also observe that the oscillations in $g(r)$ for separations greater than σ rapidly decrease to 1. Increasing the packing fraction ϕ increases the amplitudes of the oscillations, but no sharp peaks appear up to a packing fraction of $\phi = 0.502$.
The change in $g(r)$ when switching to the deformable sphere model is pictured in the panel *a* of Fig. 4.2. It can be seen that for reduced stiffness (i.e. smaller $\beta\kappa$) the discontinuity at $r = \sigma$ is softened and smaller particle separations are accessible. On the other hand a change in the stiffness of the particles has no visible impact on the form of the oscillations at larger distances.

As a next step we investigate the extent of deformation of our particles for given stiffness and packing fraction. Relevant for this distribution is the energy penalty for

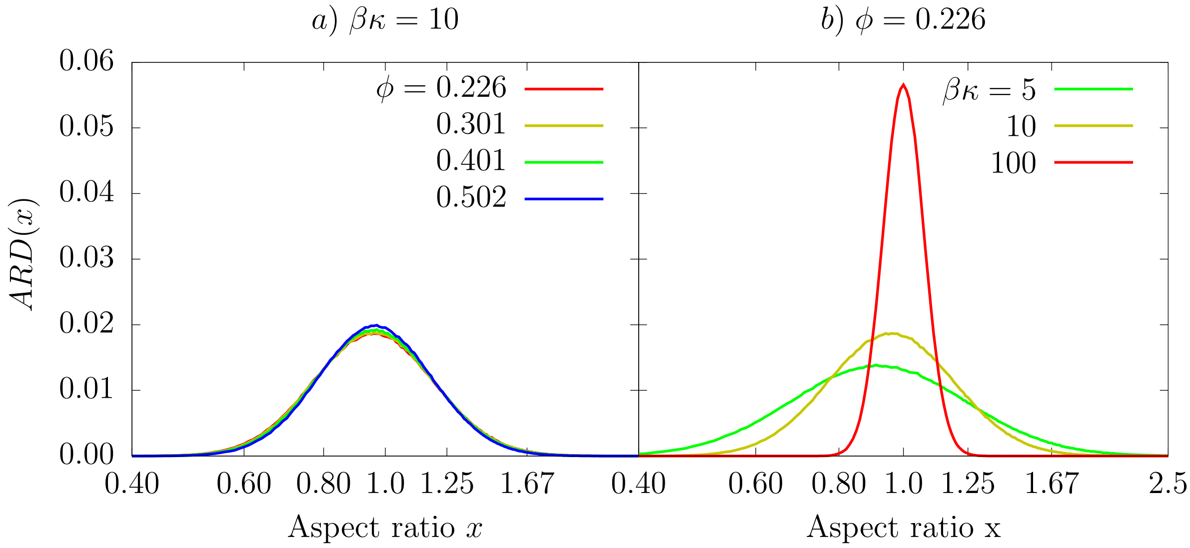

Figure 4.3: Distribution of the aspect ratio of the deformable spheres. Panel a for selected packing fractions ϕ (as labeled), with a fixed stiffness of $\beta\kappa = 10$. Panel b for decreasing stiffness $\beta\kappa$ (as labeled) with packing fraction $\phi = 0.226$.

particle deformation which we introduced in Chapter 2 in Eq. (2.9).
In Figure 4.3 the distribution of the aspect ratio of the particles is depicted. As a reminder, the aspect ratio $x = a/c$ is the relation between the two semi axis lengths a, c of the spheroid. The distribution has a maximum at $x \approx 1$ which means that in general a spherical shape is preferred. This is simply induced by our potential which is set in a way to retract the particle elongation to that of a simple sphere if there is no additional benefit of deformation.

Panel a of Figure 4.3 displays the aspect ratio distribution for different packing fractions at a fixed stiffness of $\beta\kappa = 10$. There is no visible influence of the packing fraction on the distribution, which implies that there are no additional benefits of taking on a non-spherical form in the fluid phase, except the natural thermal fluctuations.
In Panel b of Figure 4.3 the effect of reducing $\beta\kappa$ on the distribution of aspect ratio is pictured. The packing fraction is fixed at $\phi = 0.226$. For bigger values of $\beta\kappa$ the particles get stiffer and they are mainly spherical, deviations from $x = 1$ are therefore minimal. In contrast, reducing stiffness enables the particles to access regions of greater deformation. This means greater fluctuations in shape happen during the simulation since the energy penalty is smaller.

The last correlation function which was calculated for the examination of the static structure of the system is the static structure factor given in Eq. (3.23). It is displayed in Fig. 4.4. In Panel a the SSF for different packing fractions at fixed $\beta\kappa = 10$ is pictured. The most important aspect of the SSF here is the height of the first peak. It increases with increasing packing fraction and once it passes a height of ~ 3, the system undergoes with a high probability a transition to a crystalline state. This criterion is commonly known as the "Hansen-Verlet criterion" [4].
In our system the first peak stays below 3 which indicates, that the system remains in a fluid state for packing fractions up to $\phi = 0.502$ (i.e. in the next Chapter we will see that depending on the stiffness we only observe signs of an ordered state starting from

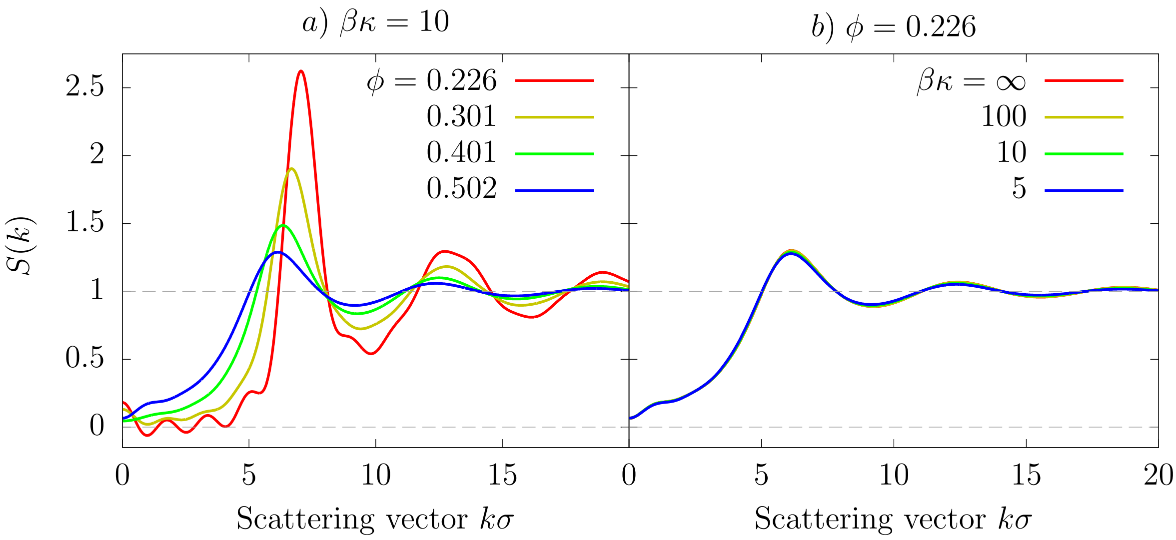

Figure 4.4: Static structure factor $S(k)$ as a function of k for a liquid system of deformable hard spheres. Panel a for selected packing fractions (as labeled) with a stiffness of $\beta\kappa = 10$. Panel b for decreasing stiffness $\beta\kappa$ (as labeled) with packing fraction $\phi = 0.226$.

$\phi = 0.52$).
Panel b of Figure 4.4 depicts the behavior of the static structure factor for a fluid system ($\phi = 0.226$) with stiffness $\beta\kappa \in [\infty, 100, 10, 5]$. For a system in a fluid state no effect of the deformability on the form of $S(k)$ is observed.

4.2 Dynamic properties

In our system we also want to identify phenomena like dynamic arrest, confinement or simply free propagation, which cannot be observed via the static structure of the system. In an effort to observe these traits we will now analyze the dynamic properties of our system.
We start with the mean squared displacement (see Eq. (3.25)) and then give a short overview over the intermediate scattering function (see Eq. (3.29)). We consider various packing fractions and stiffnesses of the particles in order to obtain an overview on the impact of deformability on the dynamic behavior of fluids.

As mentioned in Subsection 3.3.3 the MSD is a convenient tool for identifying which type of particle motions is found in a given system. To be more specific we search for characteristic changes in the MSD for different system parameters: free unrestrained motion, caging or complete confinement. How these different scenarios can be identified will be examined during the discussion of dynamical properties in the current and the next Chapter (i.e. Subsection 5.2). Further in Chapter 6 we will investigate another aspect of a system, namely dynamic arrest. However, first we will have a look at only these sparsely packed systems.

Figure 4.5 shows the MSD for three such sparsely packed configurations for three

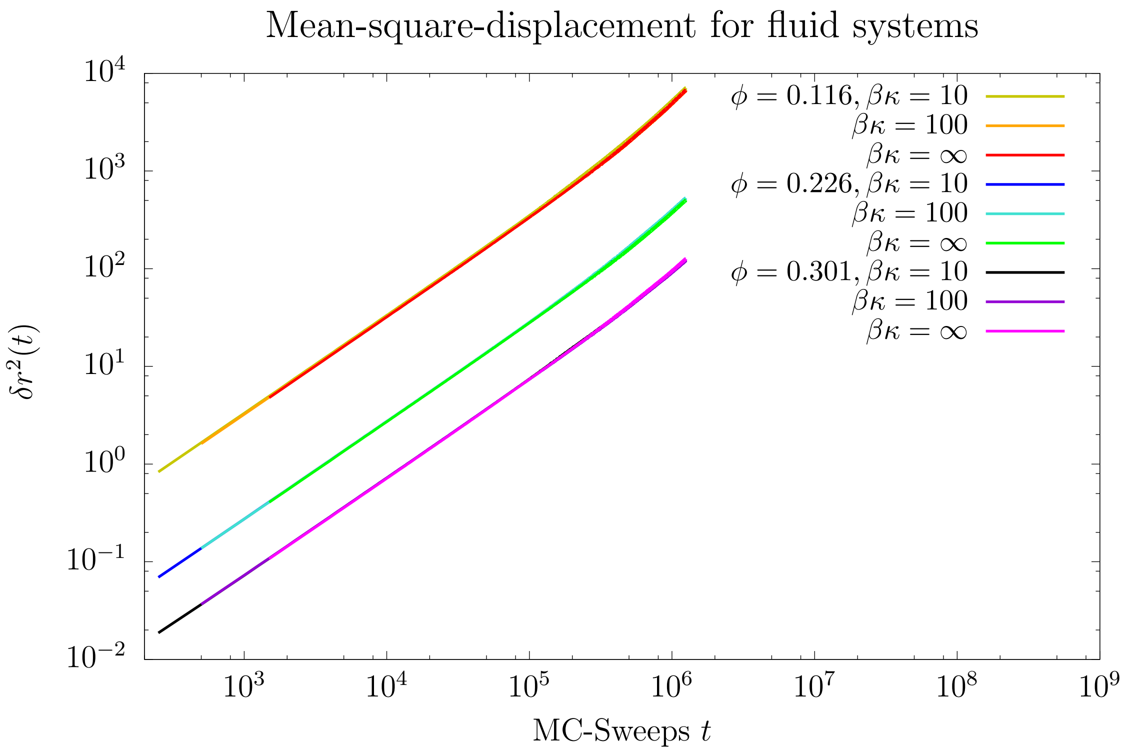

Figure 4.5: Comparison of the MSD $\delta r^2(t)$ for systems of deformable hard spheres in the fluid phase for different stiffnesses $\beta\kappa \in [\infty, 100, 10]$ (as labeled) at packing fraction fractions $\phi \in [0.116, 0.226, 0.301]$ (as labeled) as a function of Monte-Carlo-sweeps t.

different values of the stiffness $\beta\kappa$, respectively. For all datasets we observe a slope of the MSD ~ 1 characteristic for the regime of normal diffusion (see Subsection 3.3.3). This implies that particles have the possibility to move unrestrained through the system, which strengthens our assumption of fluidity taken from the static structure of sparse packed systems. We observe no signs of confinement or caging effects by other particles. However, we can also observe that for increasing packing fraction the MSD and therefore the distance that the particles can propagate on average is decreasing, which seems to be natural as the available space is decreased for increasing packing fraction, while the system still stays in the fluid phase. At those densities the deformability of the particles has no distinct influence on their capability to move through their surrounding.

Finally we take a look at the ISF for the sparsely packed systems. Similar as for the MSD the different types of motions manifest in different kinds of structural relaxations in the ISF. In general, as already mentioned in Subsection 3.3.4, the ISF encrypts how correlations between particle positions evolve as the time progresses. System often show a pattern of "one-step" relaxation or "two-step" relaxation which is a sign for caging. Further we search for incomplete relaxation (relaxation of $F_s(k,t) > 0$ for arbitrary times) which is an indicator for a crystalline structure. The importance of the IFS for this thesis is not as high as the one of the MSD, but since the topic is analyzing the structure on motions of particles it shall be discussed nonetheless. However, this function will be mainly used to underline the conclusions drawn from the MSD and its logarithmic derivative $z(t)$.

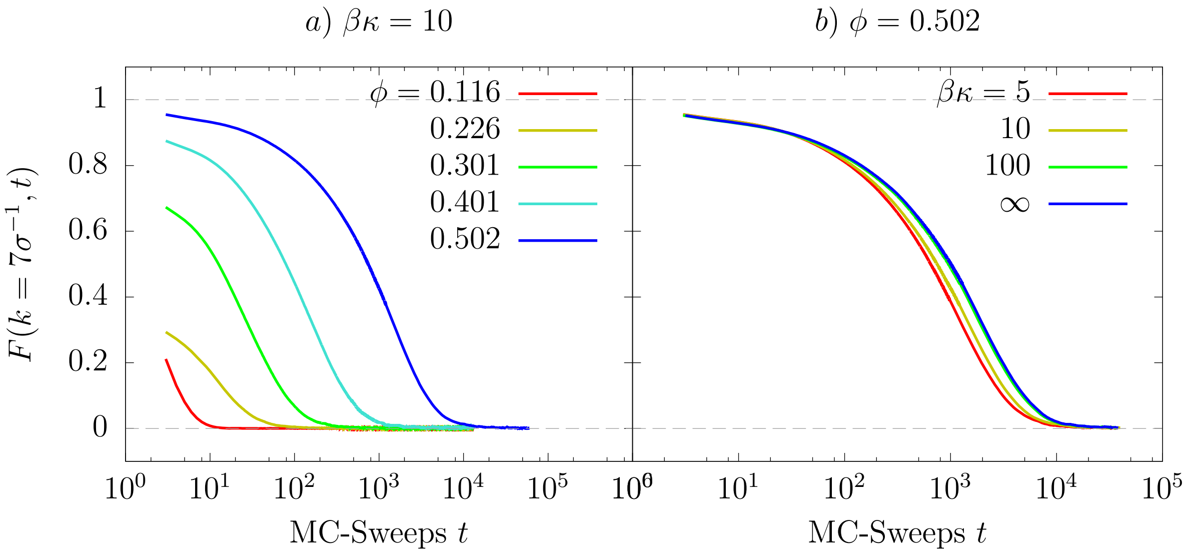

Figure 4.6: Self intermediate scattering function $F(k, t)$ at the maximum of the structure factor $k = 7.0$ as a function of MC-sweeps t for systems of deformable hard spheres. Panel a for selected packing fractions (as labeled) with a stiffness of $\beta\kappa = 10$. Panel b for increasing stiffness $\beta\kappa$ (as labeled) with packing fraction $\phi = 0.502$.

Figure 4.6 shows the IFS for a variety of sparsely packed systems and different values of stiffness. We observe an increasing time required for complete relaxation but for the shown packing fractions we observe no signs of caging or crystallinity. Panel b of Figure 4.6 also demonstrates the influence of deformability onto the IFS. We find that at relatively high packing fractions a slightly decreasing relaxation time for smaller stiffness $\beta\kappa$ is observed. This means that at these densities changes in the value of stiffness have an impact onto the capability of the particles to reach an equilibrium state.

CHAPTER 5

Ordered phase

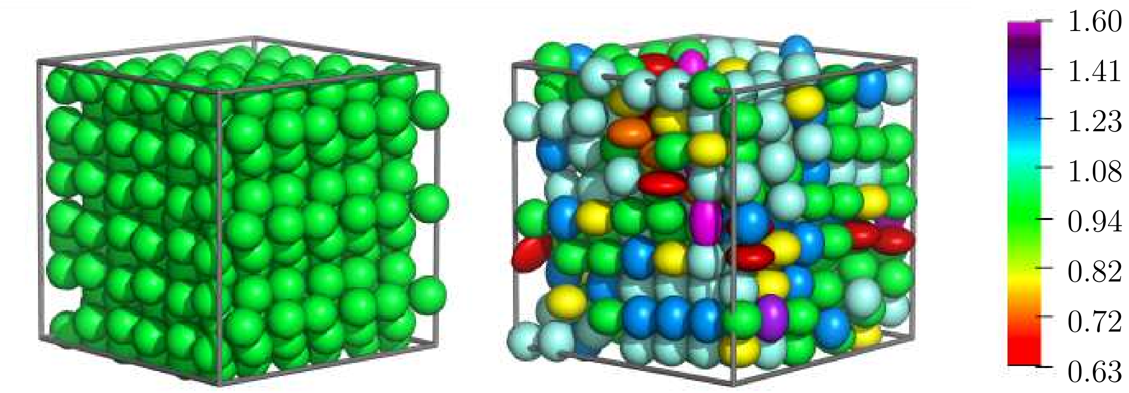

(a) Spheres (b) Spheroids

Figure 5.1: Two snapshots of a system in an ordered phase at a packing fraction of $\phi = 0.680$ (a) - rigid spheres (i.e. $\beta\kappa = \infty$) and (b) - deformable spheres (with $\beta\kappa = 5$). In the latter case the particles are colored according to their aspect ratio, red for highly oblate, green for spherical, violet for highly prolate form, covering all the colors of the rainbow.

When cooling a system rapidly below a certain temperature, a metastable, amorphous state will be formed which is known as glass; the related transition is therefore called glass-transition. Since it is amorphous (i.e. disordered) no long-range correlations between the particle position is observed, the slowed down dynamical properties of an amorphous system distinguish it from a fluid state.

In contrast, when cooled down slowly a fluid system can form a stable phase with long-range correlations. Systems consisting of hard spheres form a face-centered cubic state with a maximal packing fraction $\phi \sim 0.7405$.
For hard particles the state of the system is controlled by its packing fraction. As we have seen in the previous Chapters, our system of deformable hard spheres exists in a fluid state up to a packing fraction of $\phi = 0.502$. Therefore, we will now take a look at systems with a higher packing and we will analyze the effect of deformability on the emerging phases and their properties.

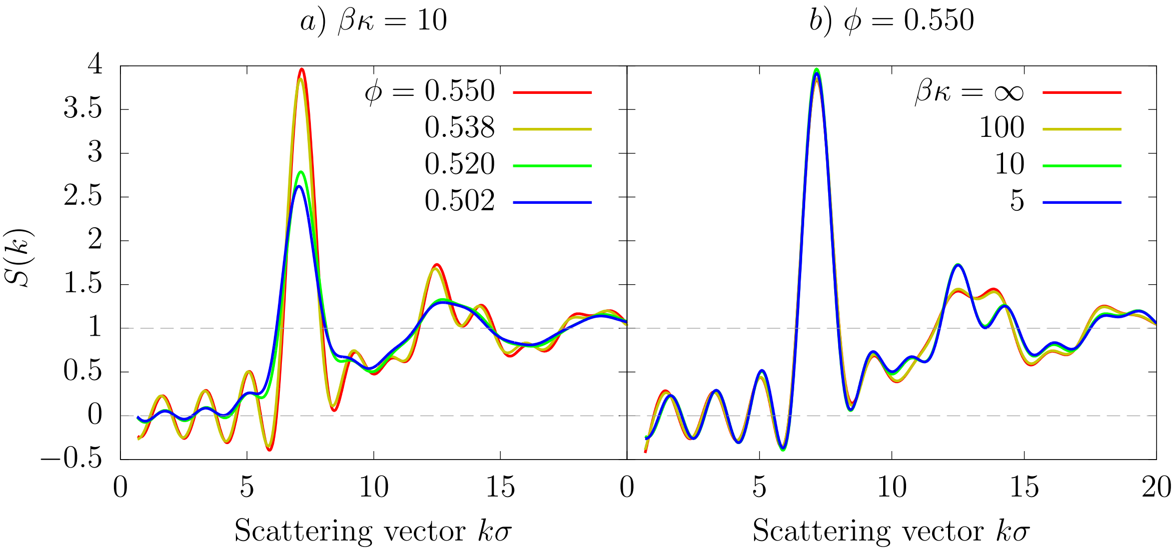

Figure 5.2: Static structure factor $S(k)$ of a system of deformable hard spheres as a function of k in units of σ. Panel a) for selected packing fractions ϕ (as labeled) with a fixed stiffness of $\beta\kappa = 10$. For ϕ between 0.520 and 0.538 a strong increase in the height of the first peak above 3 is visible, indicating a transition to an ordered state. Panel b results for fixed $\phi = 0.550$, for different packing fractions (as labeled).

5.1 Static structure

An excellent first indicator for a possible phase transition to an ordered phase is again the static structure factor $S(k)$. It is shown in panel a of Figure 5.2 for packing fractions ϕ ranging between 0.502 and 0.550 for a fixed value of stiffness $\beta\kappa$. We observe a strong increase in the height of the first peak for packing fractions between 0.520 and 0.538; this maximum reaches a height of ~ 4 which is above the Hansen-Verlet threshold [4], thus indicating the emergence of a crystalline state or of possible transient crystallites.
Panel b of Figure 5.2 shows the effect of the deformability of the particles on the shape of the static structure factor for fixed packing fraction ϕ. We observe in contrast to the fluid state of the system a different manifestation of the second and third peak of the static structure factor, but it gives no further indication on possible changes or a regression to a complete fluid state for higher deformability.

In order to examine the specific structure of the emerging ordered phase we need to resort to further post-processing tools we discussed in Chapter 3. The simplest way to identify a possible ordered structure of a system is by calculating its radial-distribution function $g(r)$: If the system is completely ordered $g(r)$ should exhibit peaks at the positions of particles in its associated primitive cell. Figure 5.3 depicts $g(r)$ for various combinations of packing fractions and stiffness parameters. In the left bottom panel of this Figure we see the change in the RDF for packing fractions ranging from $\phi = 0.502$ to 0.641. For a packing fraction of $\phi = 0.502$ $g(r)$ starts to develop a split-peak shape at $r \simeq 2\sigma$ which indicates a dense but also random packing; this peak structure gets more distinct when reaching a packing fraction of $\phi = 0.538$. Whether the system

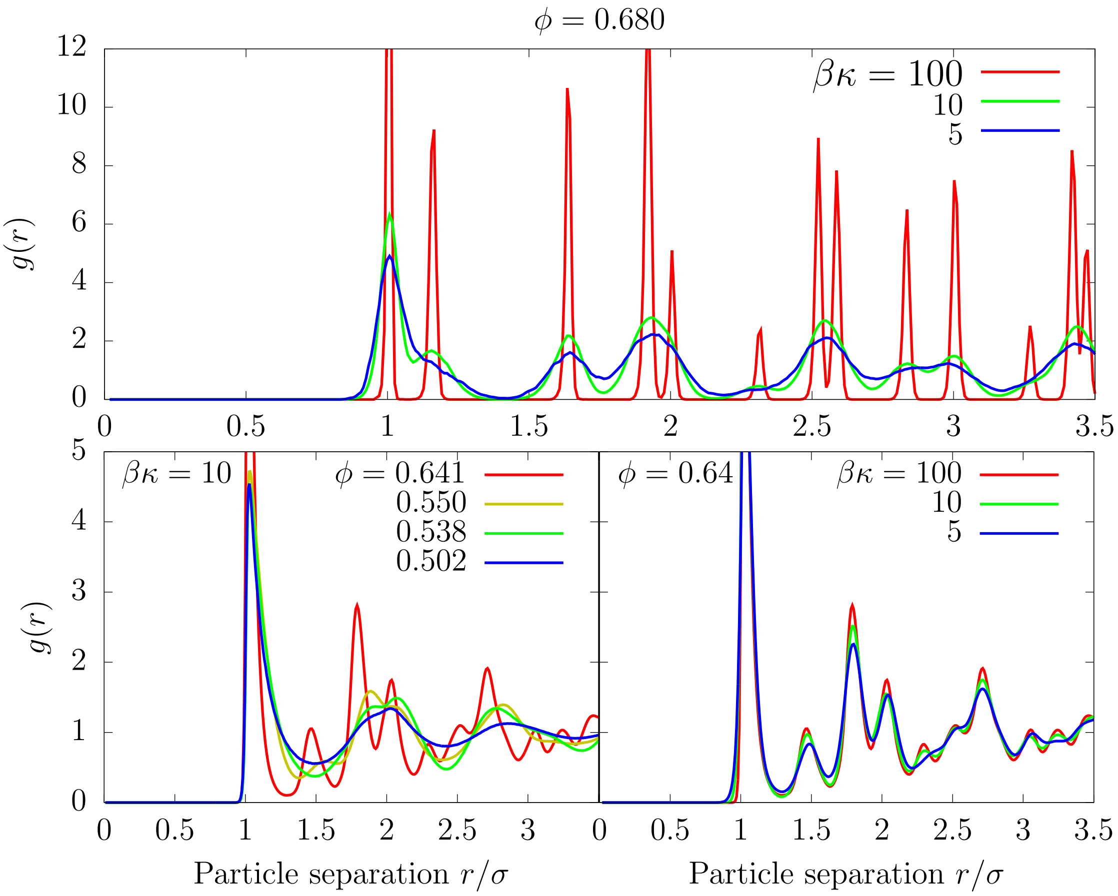

Figure 5.3: Radial distribution $g(r)$ of system of deformable hard spheres as a function of r in units of σ. Top panel for selected stiffnesses $\beta\kappa$ (as labeled) with a fixed packing fraction $\phi = 0.680$ (densest generated packing). Bottom left panel for selected ϕ (as labeled) with fixed $\beta\kappa = 10$ and bottom right panel for selected $\beta\kappa$ (as labeled) with fixed $\phi = 0.641$.

is already in a state of dynamic arrest or still in a more or less liquid state cannot be ascertained from its static structure. At a packing fraction of $\phi = 0.550$ another peak is emerging, located at the prior local minimum at $r \simeq 1.5\sigma$. Eventually we reach a possible full crystal for a packing fraction of $\phi = 0.641$ (see bottom right panel of Fig. 5.3). When analyzing the emerging sequence of peaks, we find all positions typical for a fcc-lattice: $r^{\{1\}} = \sqrt{2}\Phi$, $r^{\{2\}} = \sqrt{3}\Phi$ and $r^{\{3\}} = \sqrt{6}\Phi$, with $\Phi = \{\phi/\phi_{\text{fcc}}\}^{1/3}$ and $\phi_{\text{fcc}} = \pi/(3\sqrt{2}) \simeq 0.7405$, which indicates a full crystalline state at a packing fraction of 0.641.

Furthermore, the bottom right panel of Figure 5.3 shows the RDF for different values of $\beta\kappa$. Here we observe a slight weakening in the distinctiveness, however, the positions of the peaks are not affected by $\beta\kappa$. The small impact of the deformability on this ordered state is possibly due to the sparse packing of the system in comparison to the maximum packing ϕ_{fcc} (for spherical particles), where particles are not able to move from their position in the fcc-lattice due to a possible non-spherical shape.

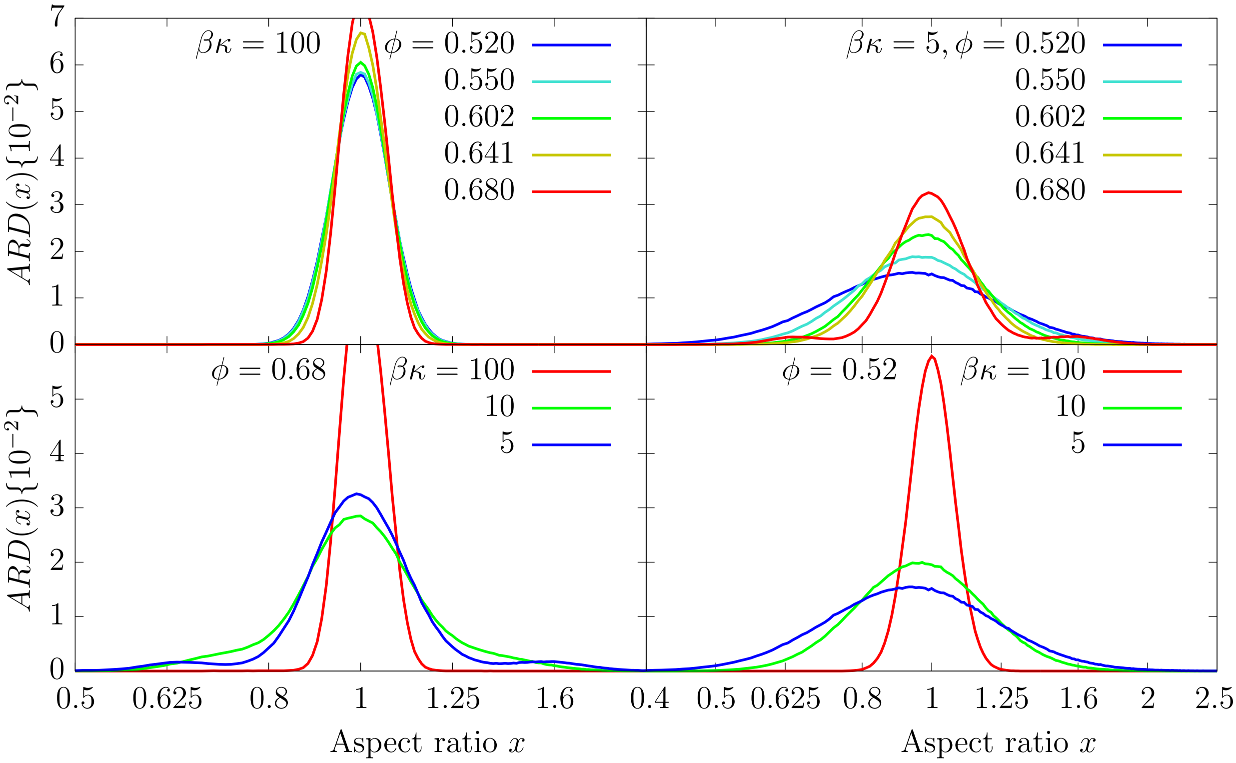

Figure 5.4: Distribution of aspect ratio of various systems of deformable hard spheres as a function of x. Top panels for selected packing fraction ϕ (as labeled) and fixed stiffness $\beta\kappa = 100$ in the left panel and $\beta\kappa = 5$ in the right panel. Bottom panels for selected $\beta\kappa$ (as labeled) with a fixed packing fraction $\phi = 0.68$ in the left panel (densest generated packing) and $\phi = 0.52$ in the right panel (coexistence of fluid and ordered state).

To underline this assumption we simulated a system starting from an initial body-centered cubic configuration. We chose this initial state of an bcc-lattice because it enables to show the effect of deformability clearly, while still retaining a reasonable simulation time, compared to a fcc-lattice configuration at high packing fractions. The top panel of Figure 5.3 shows $g(r)$ for this second crystalline state, obtained for a packing fraction of $\phi_{\text{bcc}} = \pi\sqrt{3}/2 \simeq 0.6802$. For a stiffness of $\beta\kappa = 100$, which is close to stiff particles, distinct peaks are visible in $g(r)$; they are located at distances $r^{\{1\}} = \sqrt{4/3\varPhi}$, $r^{\{2\}} = \sqrt{8/3\varPhi}$ and $r^{\{3\}} = \sqrt{11/3\varPhi}$, with $\varPhi = \{\phi/\phi_{\text{bcc}}\}^{1/3}$ and are characteristic for a bcc-lattice. When decreasing the stiffness to $\beta\kappa = 10$ we observe a smearing out of the previously well-defined peaks because of the easier deformability of the particles, which are now able to move from their lattice position. For even lower values of stiffness (i.e. $\beta\kappa = 5$) some of these peaks shrink until they are almost completely vanished.

In parallel to these structural changes we should also observe a change in the distribution of aspect ratio. It should show a form deviating from the standard Gaussian distribution with a maximum located at $x \approx 1$ (corresponding to the spherical shape). Figure 5.4 provides a comprehensive overview over the ARD for systems in a ordered state. First we take a look at the top left panel of the Figure. It shows systems with packing fractions $\phi \in [0.52, 0.68]$ for a stiffness of $\beta\kappa = 100$ (undeformable particles). We observe a weak effect of the increasing packing fractions on the ARD. The denser

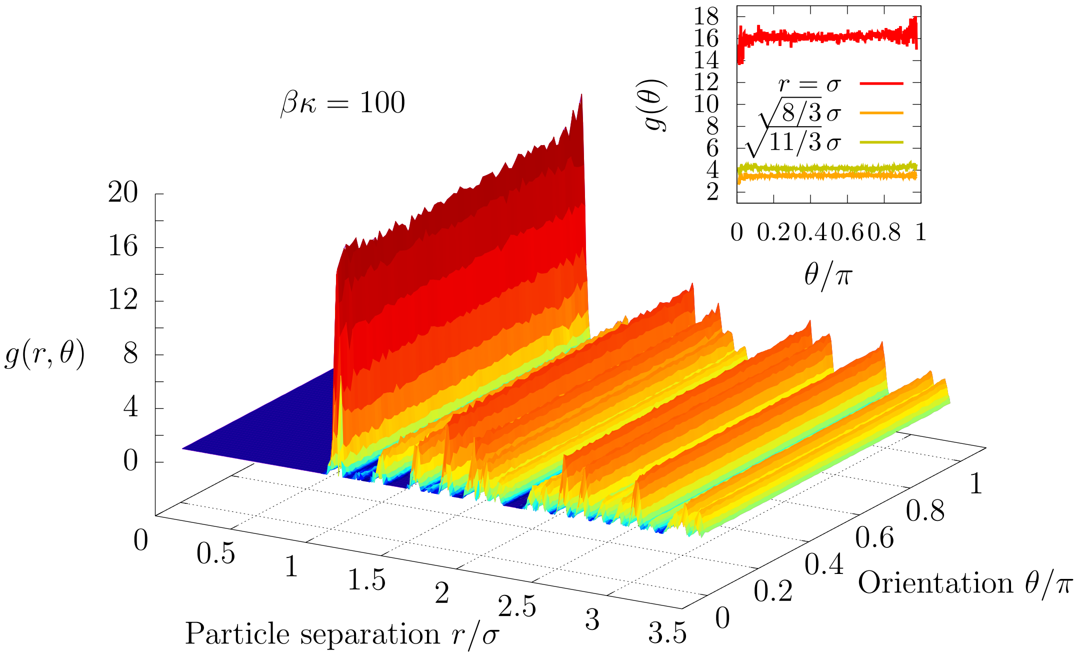

Figure 5.5: Particle-separation-orientation-distribution $g(r,\theta)$ for a system of deformable hard spheres with a packing fraction $\phi = 0.680$ and a stiffness $\beta\kappa = 100$ as a function of r and θ. The inset shows $g(r,\theta)$ as a function of θ for selected values of r (as labeled).

the system becomes, the more particles get pushed towards a complete spherical shape. This is due to the increasing confinement of the individual particles. When decreasing the stiffness to $\beta\kappa = 5$ (flexible particles) compared to our prior observations, we find a distinctively different behavior as shown in the top right panel of Figure 5.4. Again we observe a narrowing of the distributions with increasing ϕ, but they are still keeping a minimal broader shape. We also observe for the smallest packing fraction considered $\phi = 0.520$ that the maximum of the ARD is not located at $x \approx 1$.
In the bottom panels of Fig. 5.4 we fix the packing fraction ϕ and vary the stiffness $\beta\kappa$. For $\phi = 0.52$ (bottom left panel, coexistence of fluid and ordered state) we observe the same behavior as for fluid systems, the translation of the maximum and the increasing variance of the Gaussian shape. For $\phi = 0.68$ (bottom left panel) the ARD features the same static position of the maximum as for unflexible particles. Additionally two new local maxima emerge: they are located at aspect ratios $x_{\text{proplate}} \simeq 1.59$ and $x_{\text{oblate}} \simeq 0.63$ (due to the symmetry in Eq. (2.9) we expect the relation $x_{\text{oblate}} = 1/x_{\text{prolate}}$ to hold).
These different observations (i.e. the movement of the maximum and reduction of variance) indicate that the shape and maximal aspect ratio particles can assume is controlled by the increasing confinement at higher packing fractions. Further the development of specific secondary maxima indicates that the particles adapt to this limitation to gain mobility.

When looking back at our observations on the RDF at the beginning of this chapter we still have relatively well-defined major peaks (related to the bcc-lattice) even for a

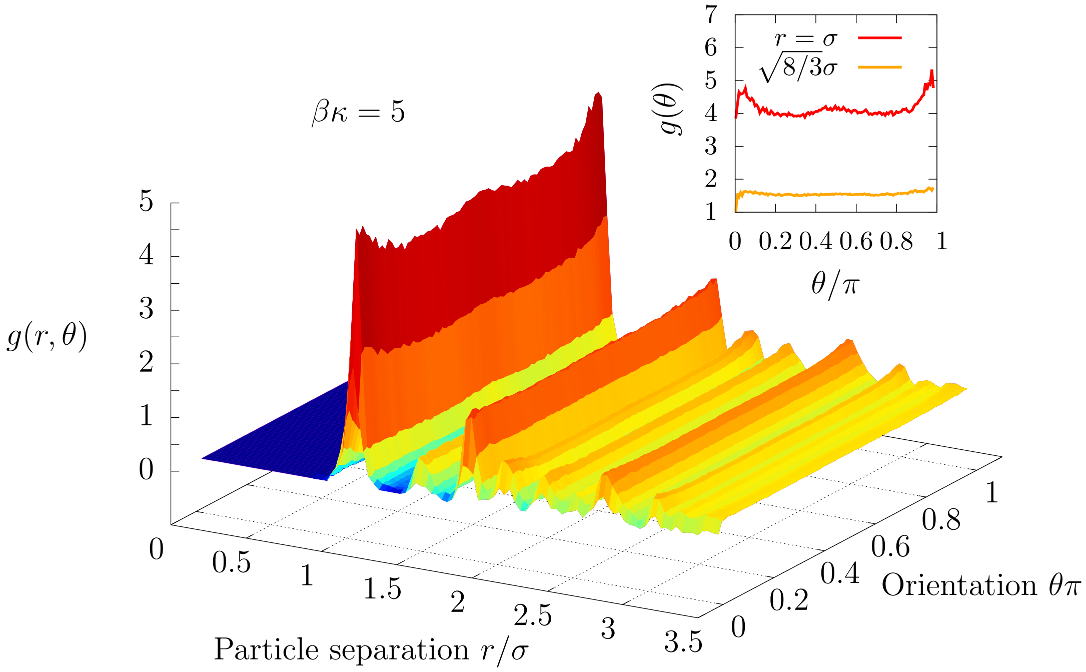

Figure 5.6: Particle-separation-orientation-distribution $g(r, \theta)$ for a system of deformable hard spheres with a packing fraction $\phi = 0.680$ and a stiffness $\beta\kappa = 100$ as a function of r and θ. The inset shows $g(r, \theta)$ as a function of θ for selected values of r (as labeled).

rather small stiffness of $\beta\kappa = 5$. Thus we should take a look at a new, now available degree of freedom of the particles, namely their orientation (see Eq. (3.19)). So far we have neglected this property since at small packing fractions there is little hope to find any correlation in particle orientations.

Figure 5.5 shows the particle-separation-orientation correlation function $g(r, \theta)$ for a system with packing fraction $\phi = 0.68$ and a stiffness $\beta\kappa = 100$. For the first three peaks we observe a uniform distribution of the orientations of the particles relative to each other (see inset): Particles are rather spherical (see also Fig. 5.4) and therefore gain no benefit from re-orienting themselves.

Figure 5.6 shows $g(r, \theta)$, now for a system at the same packing fraction $\phi = 0.68$ but for the case of more deformable particles (with $\beta\kappa = 5$). The peaks in $g(r, \theta)$ which were pronounced for the case of $\beta\kappa = 100$ are now smoothened out, some others vanished completely (see Fig. 5.3 top panel). But there are still two highly correlated and therefore preferred inter-particles distances in the pair-correlation function (see inset of Fig. 5.6). We observe a distinct non-uniform distribution for particles separated by the particle diameter σ (touching particles) and the same weakened distribution at the distance of $\sqrt{8/3}\sigma$ (corresponding to a distance of nearest neighbors in a bcc unit cell). The orientations assumed with the highest probability are $\theta = \pi \equiv 0$ and $\pi/2$. This and our observation of the emergence of secondary peaks in the ARD for increasing ϕ indicate transient localized phase transitions to a denser state not accessible by spherical particles

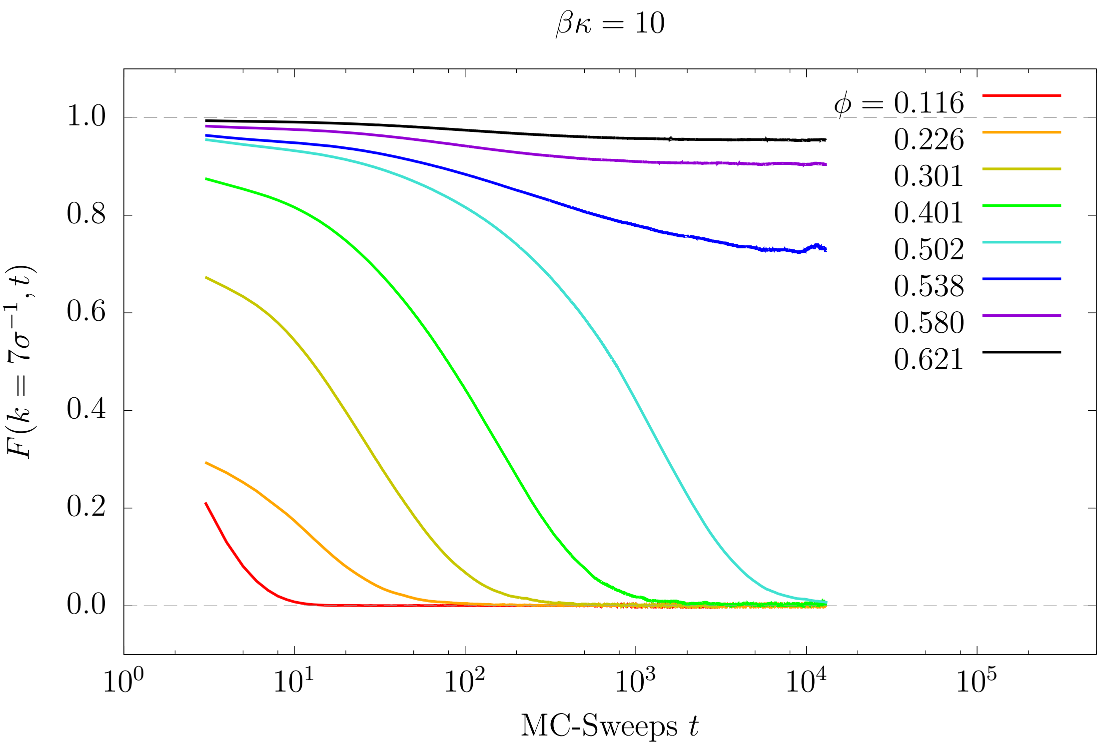

Figure 5.7: Self intermediate scattering function $F(k, t)$ for a system of deformable hard spheres for selected packing fractions (as labeled) and a stiffness $\beta\kappa = 10$ at the maximum of the structure factor $k = 7.0$ as a function of t.

[2]. In this state particles crystallize, while being oriented exactly by $\theta = 0\,(\pi)$ in the same layer of the crystal and by $\theta = \pi/2$ towards particles in neighboring layers. When reaching the highest packing fraction the spheroids take on a aspect ratio of $x = \sqrt{3}$. To observe a more distinct or even complete transition to this state of ellipsoidal packing with $\phi_{dense} \approx 0.77$ we need to access even higher packing fractions which wont be discussed during this work. For further information concerning this state please refer to [2].

5.2 Dynamic properties

Finally in this chapter we will analyze the dynamic properties. By finding at which packing fractions signs of dynamic arrest or caging set in and for which values of ϕ the particles get completely trapped, we can solidify our previous conclusions.

In Figure 5.7 the ISF is shown for a comprehensive range of packing fractions. Starting at $\phi = 0.116$ for which, as we saw in the Chapter 4, the system is in a fluid phase. The densest system has a packing of $\phi = 0.641$ at which one should already have a full solid phase following the result we found by analyzing the static structure. Hence, we observe a full relaxation of the dynamics for low values of the packing fraction; from $\phi = 0.401$ onwards we observe first caging effects in the ISF indicating short local confinement of particles by "cages" created by their surrounding neighbors.

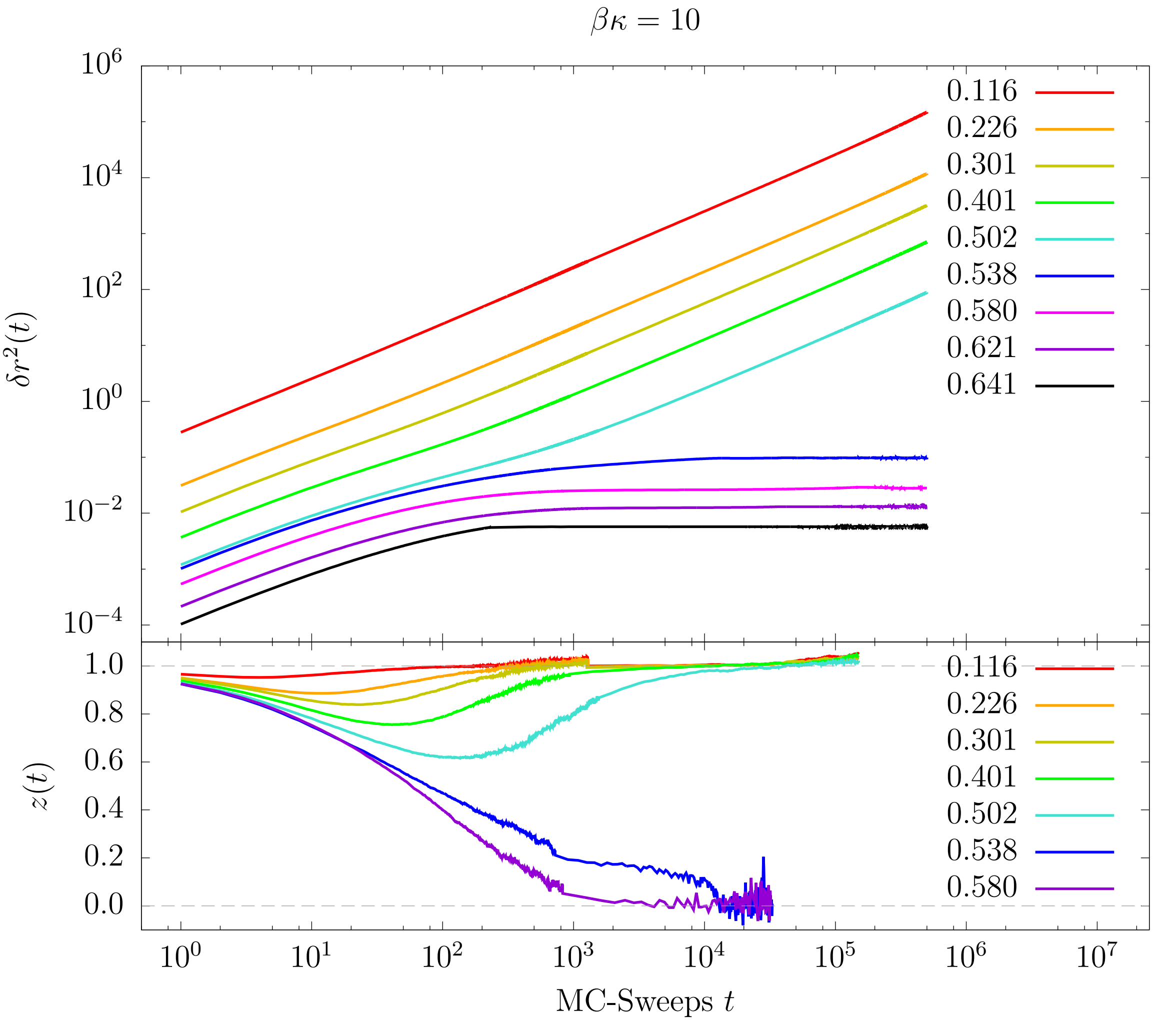

Figure 5.8: Mean squared displacement $\delta r^2(t)$ for a system of deformable hard spheres for selected packing fractions (as labeled) and a fixed stiffness $\beta\kappa = 10$ as a function of t.

At $\phi = 0.538$ the ISF shows no complete relaxation to 0 which, as mentioned in the end of the last chapter, is a sign of a transition to an arrested state. This underlines our conclusion of a phase transition happening in the range $\phi \in [0.520, 0.538]$ as concluded from the static structure. For higher packing fractions the system is completely arrested.

Finally and in order to complete our understanding of the transition into an arrested or solid phase we have calculated the mean-squared displacement $\delta r^2(t)$ for a variety of packing fractions and a stiffness of $\beta\kappa = 10$. The results are shown in Figure 5.8. We have also included the logarithmic derivate of the MSD $z(t)$ (see Eq. (3.27)) in the bottom panel to get a better understanding of the changes and transition.
For small packing fractions ($\phi \in [0.116, 0.301]$) we observe normal diffusion with $z(t) \approx 1$, i.e. typical for system in the fluid phase and unrestrained motion. At intermediate values of ϕ we see that $z(t)$ shows two regimes of diffusion: $z(t)$ first decreases in an intermediate time-regime and then tends towards unity. This particular shape is a sign of temporal caging in the system. For a packing fraction above $\phi = 0.520$ we observe $z(t) = 0$ which indicates a complete confinement of the particles. This reinforces our assumptions put forward in the previous section.

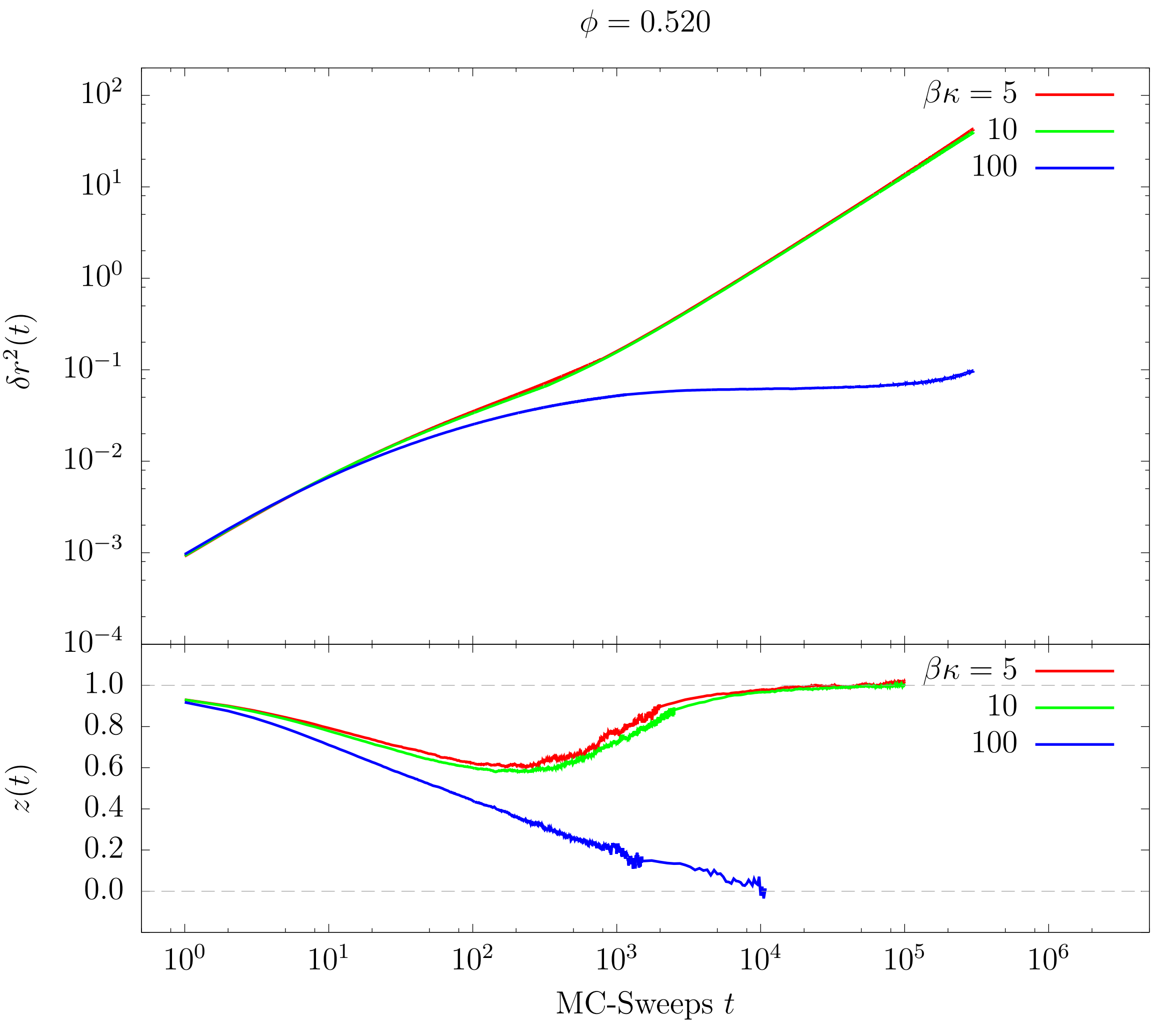

Figure 5.9: Mean squared displacement $\delta r^2(t)$ and its logarithmic derivate $z(t)$ for a system of deformable hard spheres for selected stiffnesses (as labeled) and a fixed packing fractions $\phi = 0.520$ as a function of t.

To get a complete picture of the dynamics of a DHS-system we are still missing an analysis of the effects of deformability on the MSD. We observed in Chapter 4 that for a system in an unordered state with a packing fraction $\phi < 0.52$ the particles gain no further mobility from deforming. Hence, we will start our analysis from systems at $\phi = 0.52$ which is shown in Figure 5.9.

We observe a plateau in $\delta r^2(t)$ with a long time value of $z(t) \approx 0$ for a stiffness parameter of $\beta\kappa = 100$. As mentioned early in this chapter this indicates a system in an ordered state showing confinement. When decreasing $\beta\kappa$ (i.e. $\beta\kappa = 10, 5$) the system shows a normal diffusive behavior with a long-time value of $z(t) \approx 1$. This can be interpreted as that the state points of a DHS-system ($\phi = 0.52, \beta\kappa = 10, 5$) is still in the fluid regime while the state point ($\phi = 0.52, \beta\kappa = 100$) is located after the transition line of fluid to ordered state. This observation fits the calculations of the transition lines of the DHS-model done by Batista and Miller. For further information on this topic we refer to [2].

CHAPTER 6

Porous media

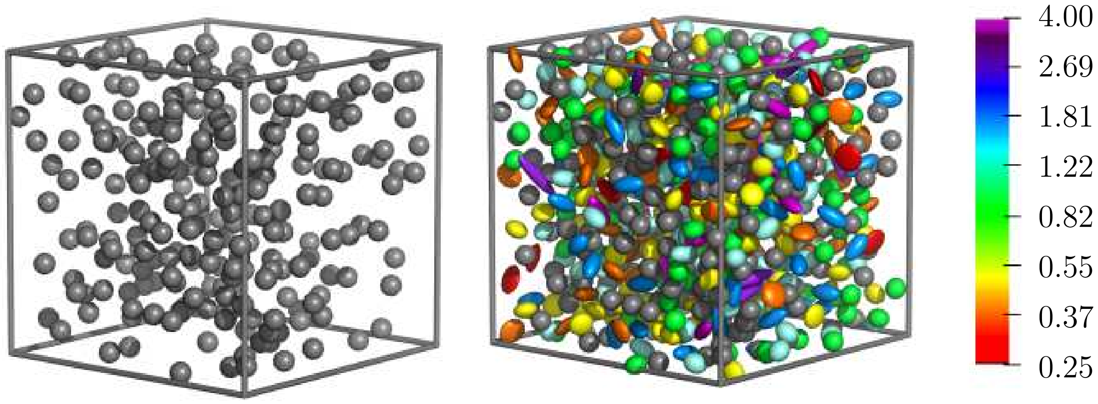

(a) Matrix (b) Immersed fluid

Figure 6.1: Two snapshots of systems illustrating the principles of the DHS-QA model. (a) - rigid spheres forming a spatially frozen matrix with a packing fraction $\phi_m = 0.10$. (b) - deformable spheres forming a fluid immersed into the matrix with a packing fraction $\phi_f = 0.20$ and stiffness $\beta\kappa = 10$. In the latter case the fluid particles are colored according to their aspect ratio, red for highly oblate, green for spherical, violet for highly prolate form, covering all the colors of the rainbow.

For the last chapter of this thesis we want to introduce another feature to our system consisting of deformable colloids: we introduce a matrix of fixed, undeformable spherical particles. This matrix is basically a subsystem of the native system consisting of a number of "frozen" particles, fixed in space. Such matrices are often used to simulate porous media. They are encountered as rocks, clay, sand or ceramics. Porous materials play a significant role in many industrial processes, for example in the purification process of polluted water, in many chemical reactions or in silica gels. Also living cells exhibit fixed cytoskeleton structures which act as porous media for fluids of proteins floating through the cell. Summarizing there are many phenomena in nature which are essentially systems of matrix and fluid elements and which require a fundamental physical or mathematical model to be thoroughly comprehended.

In our investigation our deformable spheroids now have to move through such a matrix

configuration. We have considered the matrix particles as undeformable spheres. From now on mobile, deformable particles are called "fluid" particles and fixed, undeformable particles are called "matrix" particles.
Before analyzing the behavior of this system, a number of additional definitions and concepts are required to fully comprehend the results. They are presented in the following.

6.1 Glass transition

To understand these materials more profoundly let us first neglect porous confinement and take a look at glasses or more general, slow liquids. In the last chapter we saw that a liquid system which reaches a specific packing fraction undergoes a phase transition to a state with some kind of long-range order of the particles. When slowly cooling a liquid system such a state starts to develop in initially small regions where it may dissolve again; however, when reaching a specific critical size these regions can grow larger and finally spread throughout the whole system.

When cooled fast enough a system cannot generate local crystallites beyond the critical size and will not develop a full crystalline structure despite being dense (or cooled down) enough to reach the energetically preferred crystalline state. Such a system is called supercooled: These systems seem to behave like a solid but have no long-range structure like in the case of a fluid. The probably most important example for such a material is a glass and therefore this transition is often called "glass transition", the corresponding state is called "glassy state". It represents a *meta-stable* state of the system, further, often called "slow liquid".
The main difference between a system in a glassy and in a liquid state (despite their similar static structure) is that a glass displays a phenomenon called dynamic arrest. In other words a glass shows a specific structure which hardly changes over time (similar to a stable crystal) while a liquid changes its structure continually over time. Nonetheless a glass still reacts to many stimuli in a manner different from that of a full solid because the mentioned distinct differences in their structure. The main feature that differentiates a liquid and a slow liquid are their dynamical properties. Differences between slow liquids to full solids are found (mainly) in the static structure.

To identify whether a system has reached a state of dynamic arrest, the IFS and the MSD are again the most practical tools. When a system undergoes a transition to a glassy state, these two functions exhibit a pronounced change in their long time value. The features that identify the glassy state will be further discussed over the course of this chapter.

6.2 Theroetical concepts for the fluid immersed in the matrix

A fluid under porous confinement is able to show an entirely different behavior concerning transitions between different states and dynamic features. For example, the transition temperatures between states can be shifted, or such a transition can be possibly even completely suppressed. The most important of these features to characterize the state of the confined fluid in this Chapter is the time-dependent MSD $\delta r^2(t)$. As we have seen in Chapter 4, a system in a fluid state obeys the diffusion law (see Eq. (3.26)) with the logarithmic derivate of the MSD $z \sim 1$. In the preceding Chapter 5 we learned that for dense systems a transient subdiffusion with $z(t) < 1$ is observed, which corresponds to caging effects. In contrast to a diffusive liquid which reaches a long time value $\lim_{t\to\infty} z(t) = 1$. However there are also systems that show *anomalous* (sub-)diffusion with a long time value $0 < \lim_{t\to\infty} z(t) < 1$, such as proteins confined in cell membranes or many liquids confined in porous media. Thus we observe different kinds of manifestation of the MSD $\delta r^2(t)$ and its logarithmic derivate $z(t)$ as a function of time, depending on the environment of the particles.

In this thesis we consider equilibrated configurations. As we saw in the last chapter, a system with a sufficiently high packing fraction will always assume a crystalline state when given time to properly equilibrate. Therefore, we need a method to generate a system which remains disordered. For this purpose we use the concept of the quenched-annealed (QA) model. This model was designed to investigate systems which consist of a disordered porous matrix and an immersed fluid.

The protocol for generating such a system consists of three steps:

(i) A disordered configuration consisting of HS particles is generated where we apply periodic boundary conditions at the walls of the cubic simulation cell; these particles will represent the matrix.

(ii) These matrix particles are randomly moved according to the protocol discussed in Subsection 3.1.1 until the system is equilibrated. Then a randomly chosen equilibrium configuration is selected of these particular configurations and these matrix particles are hence forward frozen in space.

(iii) Into the matrix new HS particles are immersed; the simulation is carried on until this system reaches equilibrium with these new particles.

These steps have to be followed in order to generate a proper configuration of the HS-QA model. However, in our study we want to investigate a fluid consisting of deformable hard spheroids (instead of simple spheres) immersed into a porous matrix. Therefore we split step (iii) into the three sub-steps which we have discussed in the Subsections 3.1.1, 3.1.2 and 3.1.3. Hence in the same way as we did in Chapter 3 to define the DHS-model, we extend the HS-QA-model to the DHS-QA-model - we simulate next to translational movement, rotational movement and deformation in every step to reach an equilibrium state.

The last concept we need before analyzing our results for the DHS-QA model a theoretical theory we can use as a foundation and with which we can interpret possible changes because of the deformability of the particles. One of the most successful theories for the slowdown and dynamic arrest of glass forming systems and especially under confinement in a matrix is the replica mode-coupling theory (RMCT)[6]. We will not go into detail here since the HS-QA was already under thorough research in relation to the RMCT by [7]. But we want to use some of the predictions of the RMCT for a HS-QA system.

Basically by tracking the motion of particles through time-dependent local densities

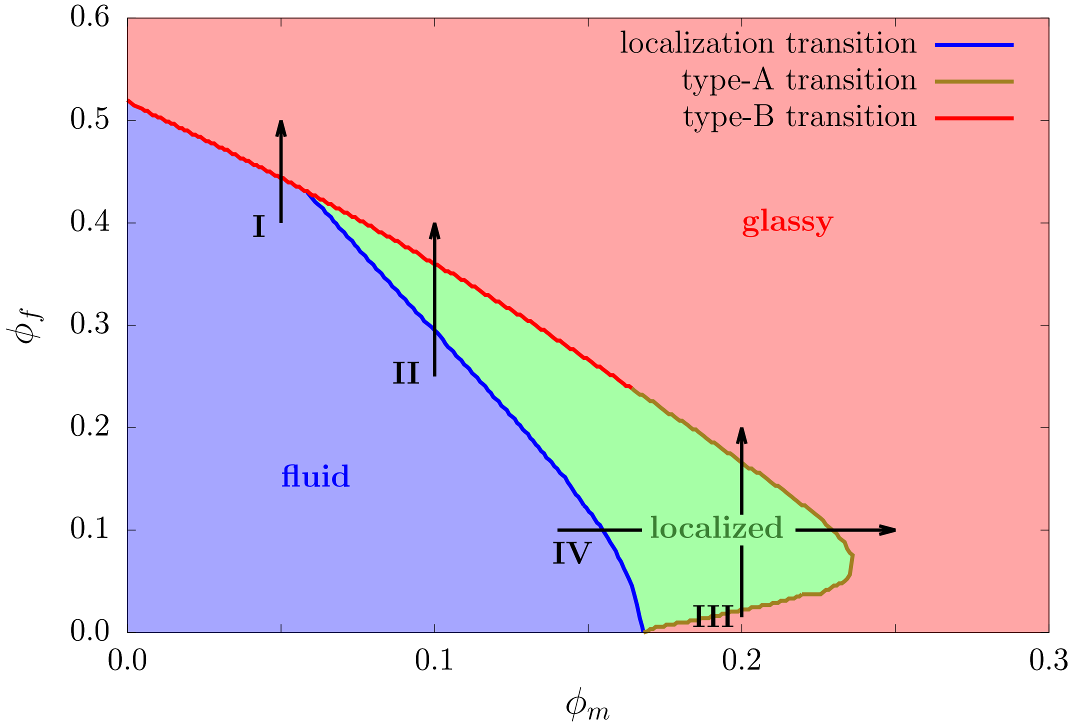

Figure 6.2: Kinetic diagram predicted by RMTC.
Depending on the packing fractions ϕ_m of the matrix and ϕ_f of the fluid, RMCT predicts HS-QA systems to assume either a fluid, localized or glassy state (blue, green and red areas in the diagram). These areas are separated by transition lines. The system can undergo either a type-A, type-B or localization transition. The black arrows indicate 4 paths chosen in this thesis to analyze this phase space. (reproduced from [7])

(Eq. (3.21)) and their correlation functions (see 3.3), the theory can make predictions about the dynamical properties and glass transitions of the system. Additionally, RMCT also predicts another type of transition which is called "localization transition".
This is another sub-characterization of the fluid (non-glassy) state which shows itself in the IFS and MSD through intermediate steps as in case of caging and especially in a non-infinite long-time value of the MSD.

6.2.1 Kinetic diagram

To get an overview of the different states in the phase space of the DHS-QA model we will use in particular the "kinetic diagram" predicted by the RCMT. It is a visualization of all possible states in the parameter space, spanned by the two parameters matrix packing fraction ϕ_m and fluid packing fraction ϕ_f. It is depicted in Figure 6.2 and shows where, according to the RMCT for the HS-QA model, the system is in a fluid, localized or glassy state (blue, green and red areas).

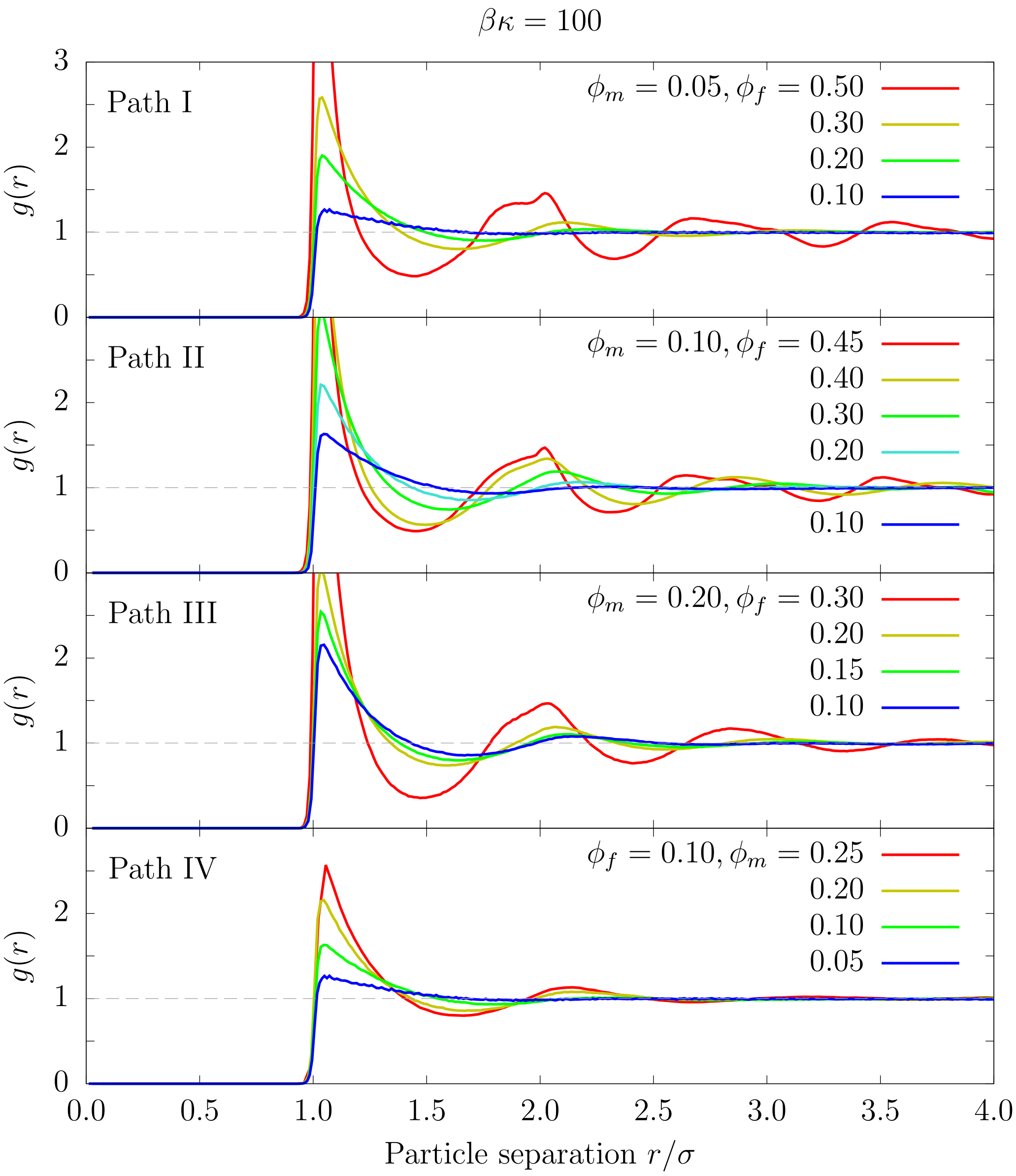

Figure 6.3: Radial distribution $g(r)$ for a DHS-QA-system calculated along the paths I-IV (as labeled) with a stiffness $\beta\kappa = 100$ and various combinations of packing fractions ϕ_m and ϕ_f (as labeled) as a function of r in units of σ.

To properly observe the different possible transitions between phases in our system and the effect of deformability on these transitions, we will follow in our investigation four paths in the kinetic diagram (black arrows in Fig. (6.2)), where each of these paths should represent a different kind of transition:

Path I: The matrix has a small packing fraction $\phi_m = 0.05$, while the fluid packing fraction is varied in the interval $\phi_f \in [0.05, 0.50]$.

Path II: The matrix has an intermediate packing fraction $\phi_m = 0.10$, while the fluid packing fraction is varied in the interval $\phi_f \in [0.05, 0.45]$.

Path III: The matrix has a rather large packing fraction $\phi_m = 0.20$, while the fluid packing fraction is varied in the interval $\phi_f \in [0.05, 0.30]$.

- **Path IV:** The fluid has a packing fraction $\phi_f = 0.10$, while the matrix packing fraction is varied in the interval $\phi_f \in [0.05, 0.25]$.

The different types of transition lines shown in Figure 6.2 (see legend) are not of high concern for the analysis in this chapter. But for purpose of completion it shall be mentioned shortly. The red line represents a type-B transition to a glassy state [7], while the green line represents a type-A transition. [7] The main difference is that in the long time value of the collective IFS for a type-B transition displays a jump when reaching the transition line, while for a type-A transition it varies continuously.

All simulations of state points along path II-IV are performed with a number of particles $N_i = 400$ per packing fraction $\phi_i = 0.1$ $(i = m, f)$. Along path I, to increase the effect of the relatively small number of matrix particles ($N_m = 200$), the number of particles is increased to twice the number $N_i = 800$ (constitutes to $N_m = 400$) per packing fraction $\phi_i = 0.1$ $(i = m, f)$. Additionally to the ensemble average (see Section 3.3) an average over 5 different matrix configurations is used for all results presented during this chapter.

6.2.2 Static structure

First of all, we have to confirm that we really operate in the domain of fluids or in the domain of amorphous systems. For this purpose, we again look at the radial distribution $g(r)$ and the static structure factor $S(k)$. When reconsidering the static structure presented in the previous chapter (Subsections 5.2 and 5.3), we saw that in case of a crystalline state we find local maxima in the RDF at positions specific for the respective structure.

In Figure 6.3 we observe none of these maxima for the states investigated in this Section. From top to bottom this Figure depicts the function $g(r)$ for each of the paths I-IV (shown in Fig. 6.2). For this case we choose a stiffness of $\beta\kappa = 100$ because it resembles an HS-system in all aspects and is therefore ideal to compare the results to the predictions made by the RMCT. Furthermore, decreasing the stiffness $\beta\kappa$ only reduces the distinctness of the extrema of the static structure further as we saw over the last chapters; this justifies our assumption that $\beta\kappa = 100$ serves as an appropriate value for representing HS-particles.

For all paths investigated we observe the typical shape of the RDF of an unordered system, which we already discussed in detail in Chapter 4. For total packing fractions (i.e. $\phi_{tot} = \phi_m + \phi_f$) below $\phi_{tot} = 0.5$, features typical for a system in a fluid-like state can be observed. As we increase the fluid packing fraction (Path I: $\phi_f = 0.5$, II: $0.4, 0.45$ and III: 0.3) we observe a splitting of the peak at the distance $r = 2\sigma$, this is an indicator of a closed randomly packed system, as it is observed in amorphous or glass-forming systems.

The static structure factor $S(k)$ is shown along the paths I-IV in Figure 6.4. As expected we observe no indicators of crystallization in the SSF. The overall shape of $S(k)$ is similar to the one discussed in Chapter 4. The height of the first peak for the highest packing fractions considered (Path I: $\phi_f = 0.5$ and II: $\phi_f = 0.45$) is near or slightly above the Hansen-Verlet threshold value of ≈ 3 [4], which indicates the possible presence of some kind of crystalline structure, while it does not suggest any kind of ordered state.

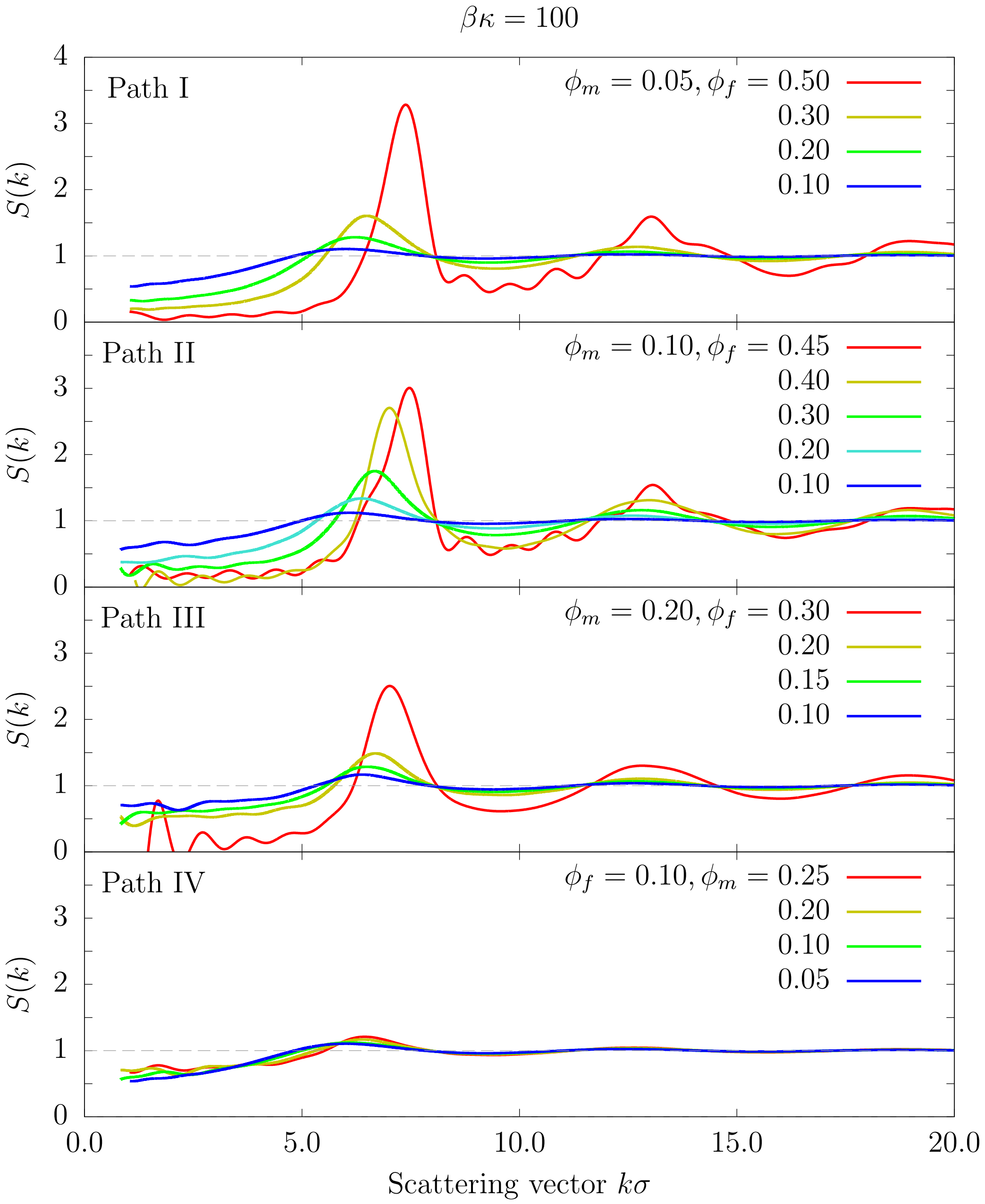

Figure 6.4: Static structure factor $S(k)$ of a DHS-QA-system calculated along the paths I-IV (as labeled) with a stiffness $\beta\kappa = 100$ and various combinations of packing fractions ϕ_m and ϕ_f (as labeled) as a function of k in units of σ.

Summarizing, $g(r)$ and $S(k)$ indicate for none of the four paths any characteristic features of crystallization. This observation underlines the assumption that even the most diluted matrix already completely suppresses the features of long-range order, i.e. of a crystalline structure.

6.2.3 Dynamic properties

Similar to the case of the DHS model (see Subsection 5.2) we will investigate the dynamic behavior of the DHS-QA system via the MSD $\delta r^2(t)$ and its logarithmic time derivate

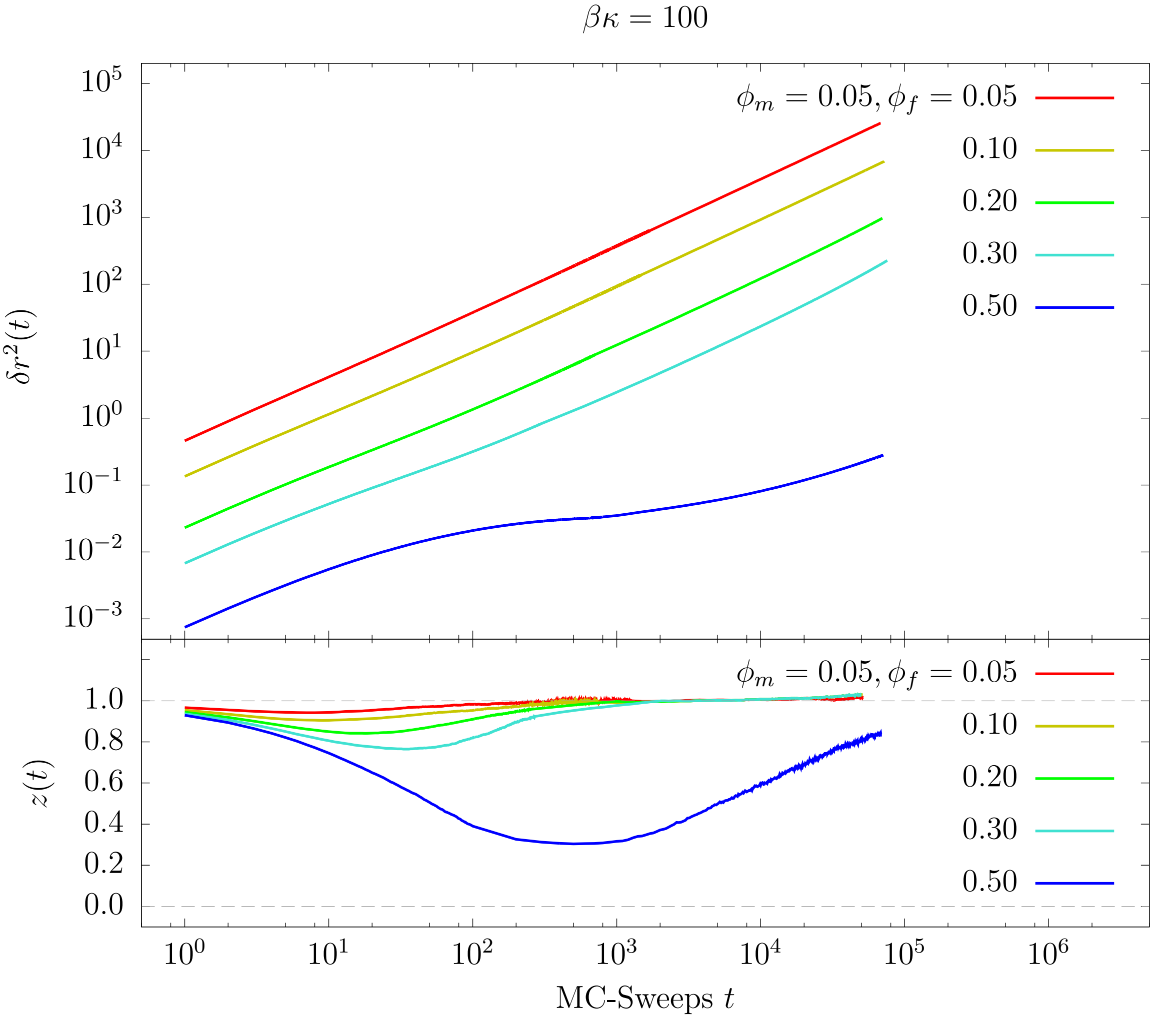

Figure 6.5: Mean squared displacement $\delta r^2(r)$ and its logarithmic derivate $z(t)$ for a DHS-QA-system calculated along path I with a stiffness $\beta\kappa = 100$ and various combinations of packing fractions ϕ_m and ϕ_f (as labeled) as a function of t.

$z(t)$. Again we will focus on the paths I-IV as they are shown in Figure 6.2.

We start with path I, results for $\delta r^2(t)$ and $z(t)$ are shown in Figure 6.5. Like already mentioned, path I follows a constant matrix packing fraction $\phi_m = 0.05$. We have to remember that in MC-simulations it is not possible to resolve the "ballistic" or "inertial" regime ($z(t) > 1$) occurring at small times. At larger time scales MC-simulations provide reliable results. We observe an initial subdiffusive ($z(t) < 1$) regime for all systems. For the smallest fluid packing fraction, $\phi_f = 0.05$, the system shows an essentially normal diffusive behaviour over the whole simulation time, which means that the particles can move through the rather dilute matrix in an unrestricted manner. As we increase ϕ_f, the system shows an increasingly strong subdiffusive regime where $z(t) < 1$. For longer simulation time the system recovers normal diffusion after about 1000 sweeps. For the highest value of fluid packing fraction, i.e. $\phi_f = 0.5$, it drops down to a value of $z \simeq 0.15$. This distinct subdiffusive behavior is due to caging effects when approaching the glass-transition. [7] Still, even in this case the system still recovers a normal diffusive behaviour after many sweeps.

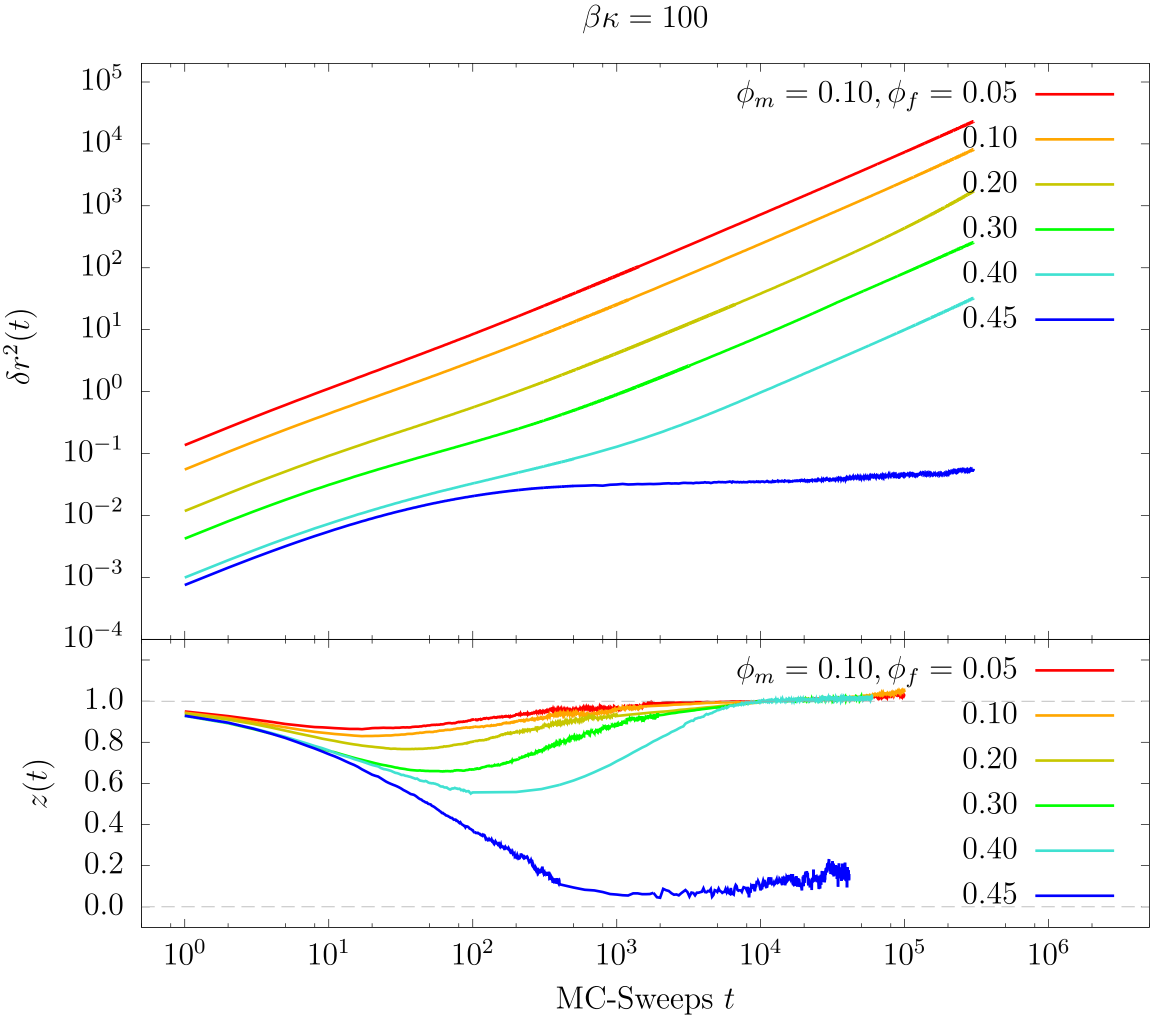

Figure 6.6: Mean squared displacement $\delta r^2(r)$ and its logarithmic derivate $z(t)$ for a DHS-QA-system calculated along path II with a stiffness $\beta\kappa = 100$ and various combinations of packing fractions ϕ_m and ϕ_f (as labeled) as a function of t.

Results for $\delta r^2(t)$ and $z(t)$ for systems along path II are visualized in Figure 6.6. Along path II the matrix packing fraction is fixed at $\phi_m = 0.10$, while the fluid packing fraction is increased up to a value of $\phi_f = 0.45$. The overall behavior of these functions looks similar to their counterparts along path I. For $\phi_f = 0.05$ the particles show a short regime of subdiffusive behavior. This subdiffusivity becomes more distinct for higher fluid packing fractions, where $z(t)$ attains values distinctively below unity.
Still for $\phi_f \in [0.05, 0.3]$ the particles always recover the normal diffusive regime for larger time scales. For a packing fraction of $\phi_f = 0.45$ there is a sudden jump in $z(t)$ a near complete confinement. This can be interpreted as the anticipated transition to a glassy state, because this goes further than simple caging effects. Most probable this is due to partly confinement of the particles of an amorphous system.

Figure 6.7 depicts the MSD and its logarithmic derivate along path III with a matrix packing fraction $\phi_m = 0.20$. Along this path a significantly different type of diffusivity is observed compared to the paths I and II. Along path III the recovery of normal diffusivity takes a much longer time. Further a temporary region of nearly constant subdiffusion is

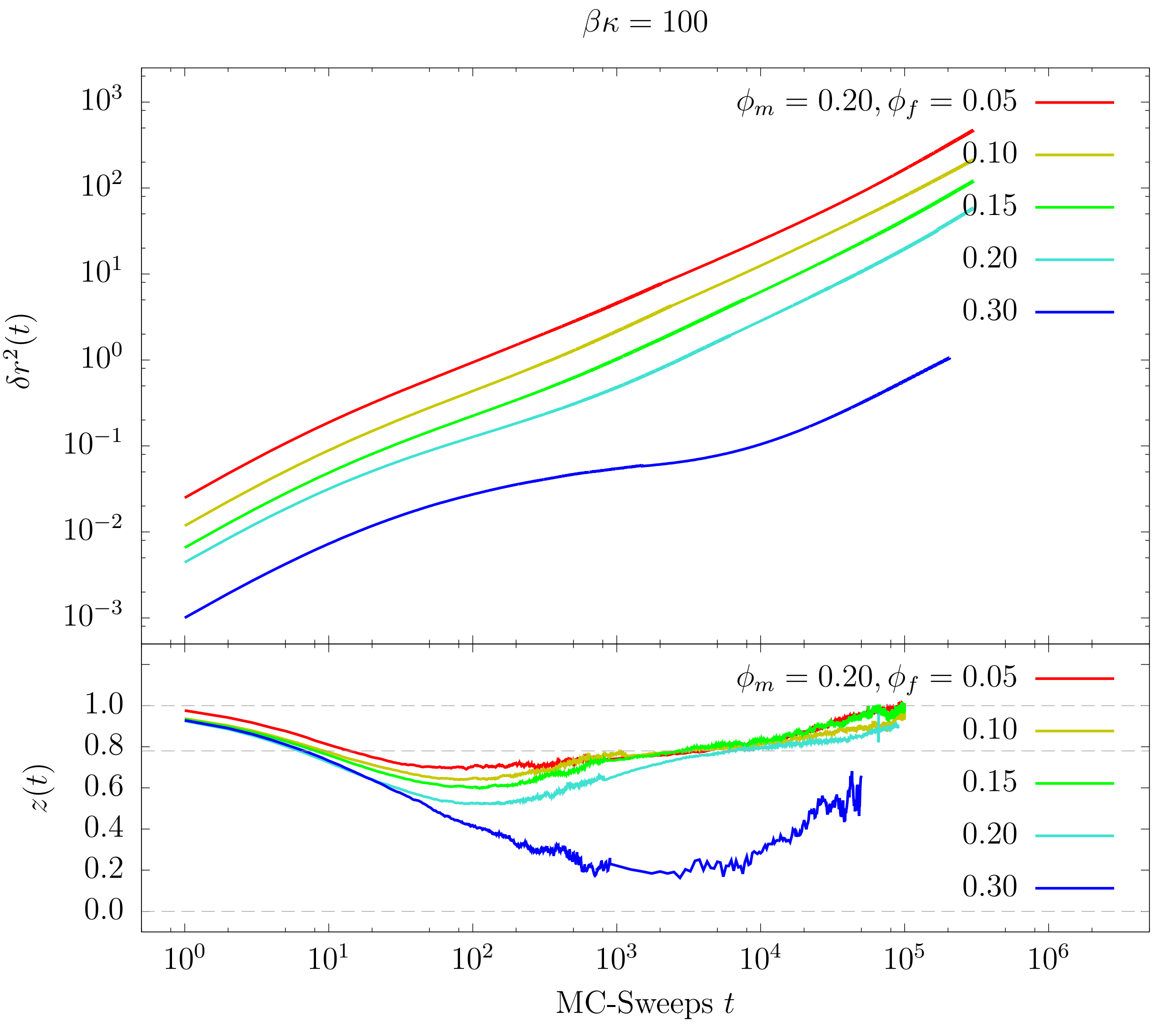

Figure 6.7: Mean squared displacement $\delta r^2(r)$ and its logarithmic derivate $z(t)$ for a DHS-QA-system calculated along path III with a stiffness $\beta\kappa = 100$ and various combinations of packing fractions ϕ_m and ϕ_f (as labeled) as a function of t.

observed as an intermediate regime; it is characterized by a value of $z(t) \simeq 0.78$ and seems to be independent of ϕ_f. This is not predicted by RMCT where the only "intermediate subdiffusive" regime is observed at $z(t) = 0.5$ (while it is completely unknown for simple glass forming systems). These features where also observed by Kurzidim et. al. [7], who investigated the dynamics of HS-QA systems through molecular dynamics simulations. They interpret this unusual behavior as to be most likely due to confinement effects becoming more important.

These confinement effects are foreign in simple glass-forming systems where only caging effects are observed. In this sense they differentiate these features by calling the initial subdiffusive regime *caging regime* and the later *the subdiffusive regime*. At last for $\phi_f = 0.30$ we observe again a jump in $\delta r^2(t)$, similar to path I, to a subdiffusive value of about $z = 0.2$, which is not completely recovered.

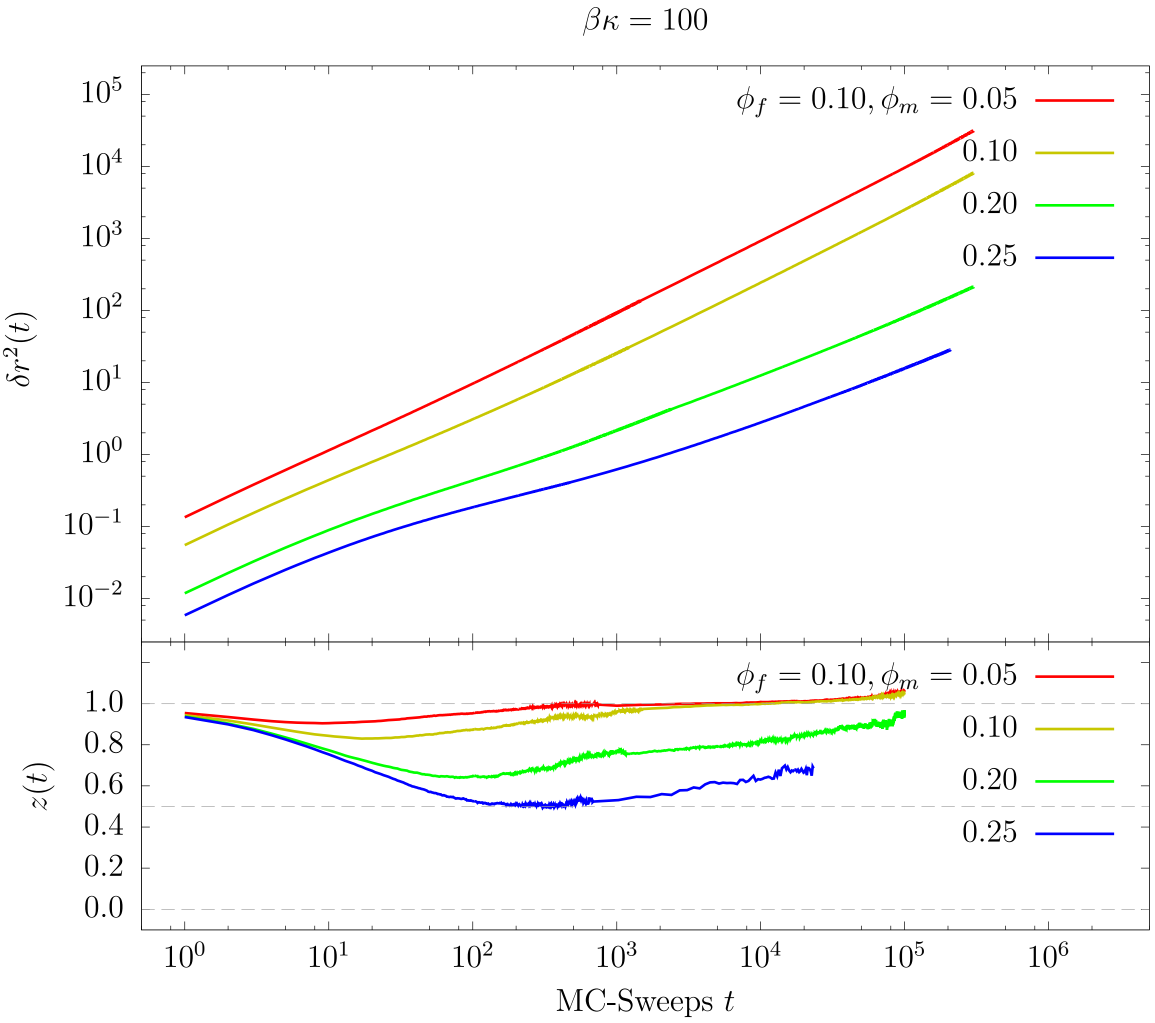

Figure 6.8: Mean squared displacement $\delta r^2(r)$ and its logarithmic derivate $z(t)$ for a DHS-QA-system calculated along path IV with a stiffness $\beta\kappa = 100$ and various combinations of packing fractions ϕ_m and ϕ_f (as labeled) as a function of t.

Finally $\delta r^2(t)$ and $z(t)$ along path IV are shown in Figure 6.8. Now the fluid packing fraction is kept constant at $\phi_f = 0.10$ while the matrix packing fraction ϕ_m is varied. We observe that all but the system with the lowest value of ϕ_m shows an initial caging regime and a subdiffusive (confinement governed) regime. For a matrix packing fraction of $\phi_f = 0.25$ $z(t)$ reaches a value as small as $z = 0.5$; over the whole simulated time normal diffusion is never recovered for this case.

When reconsidering the results of Chapter 5 we do not reach total packing fractions ϕ_{tot} high enough to observe particles in complete indefinite confinement (characterized by $z(t) \simeq 0$) due to crystallization. Further, since we observe a high impact of ϕ_m on the degree of subdiffusion and therefore the value of $z(t)$, the observed features are most probable due to the fluid particles being enclosed and confined by the local cages of matrix particles for long time scales.

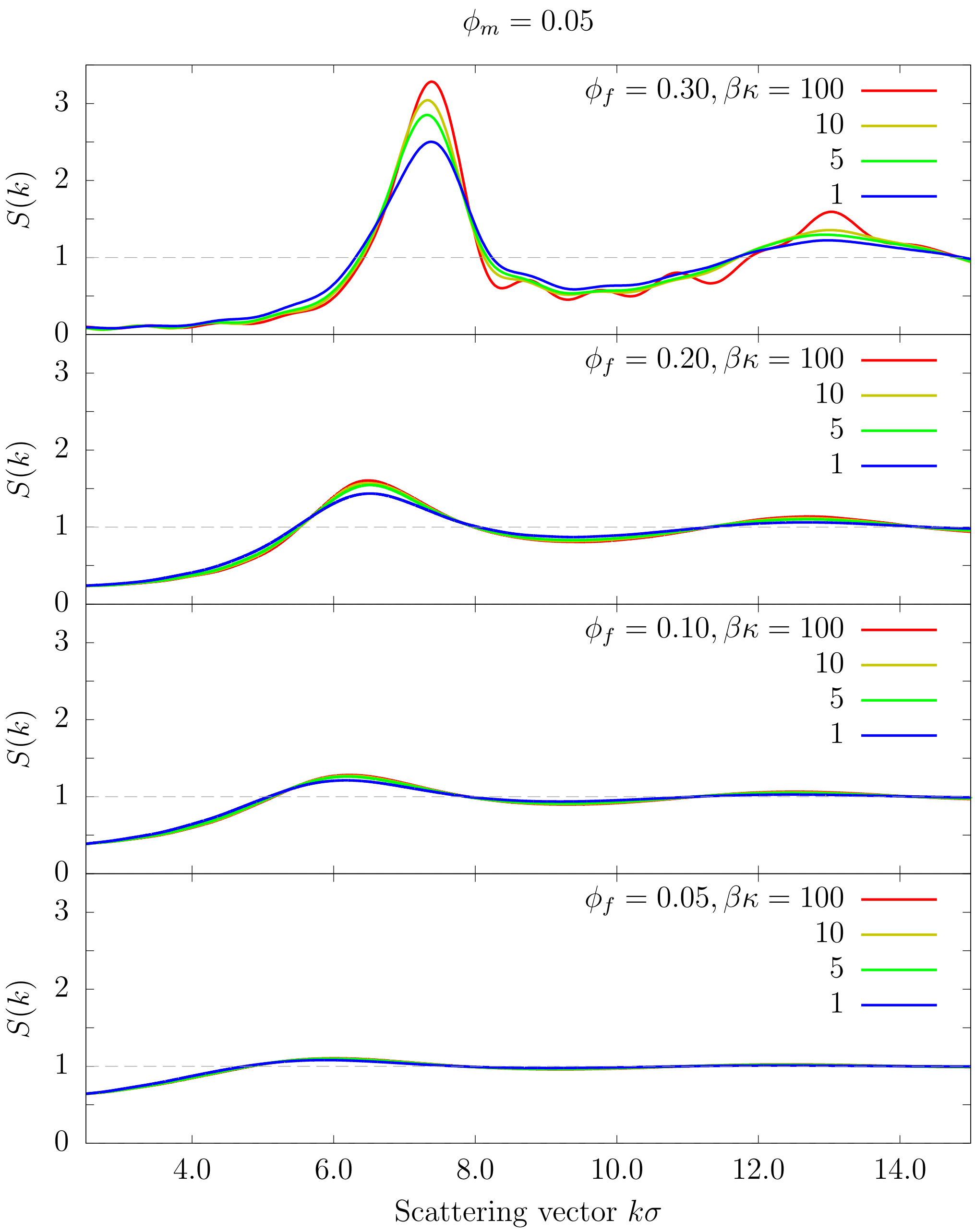

Figure 6.9: Static structure factor $S(k)$ of a DHS-QA-system calculated along path I with a matrix packing fraction $\phi_m = 0.05$ and various combinations of fluid packing fractions ϕ_f and stiffness parameters $\beta\kappa$ (as labeled) as a function of k in units of σ.

6.3 Effects of deformability under the DHS-QA model

By introducing deformability in the DHS-QA model as an additional parameter of the system, we introduce new features and new additional effects. Within the well-known framework we will look at a possible impact of the deformability on the static structure and on the dynamic behavior of the systems. In the following we will try to disconnect possible effects due to either the matrix packing fraction ϕ_m or the fluid packing

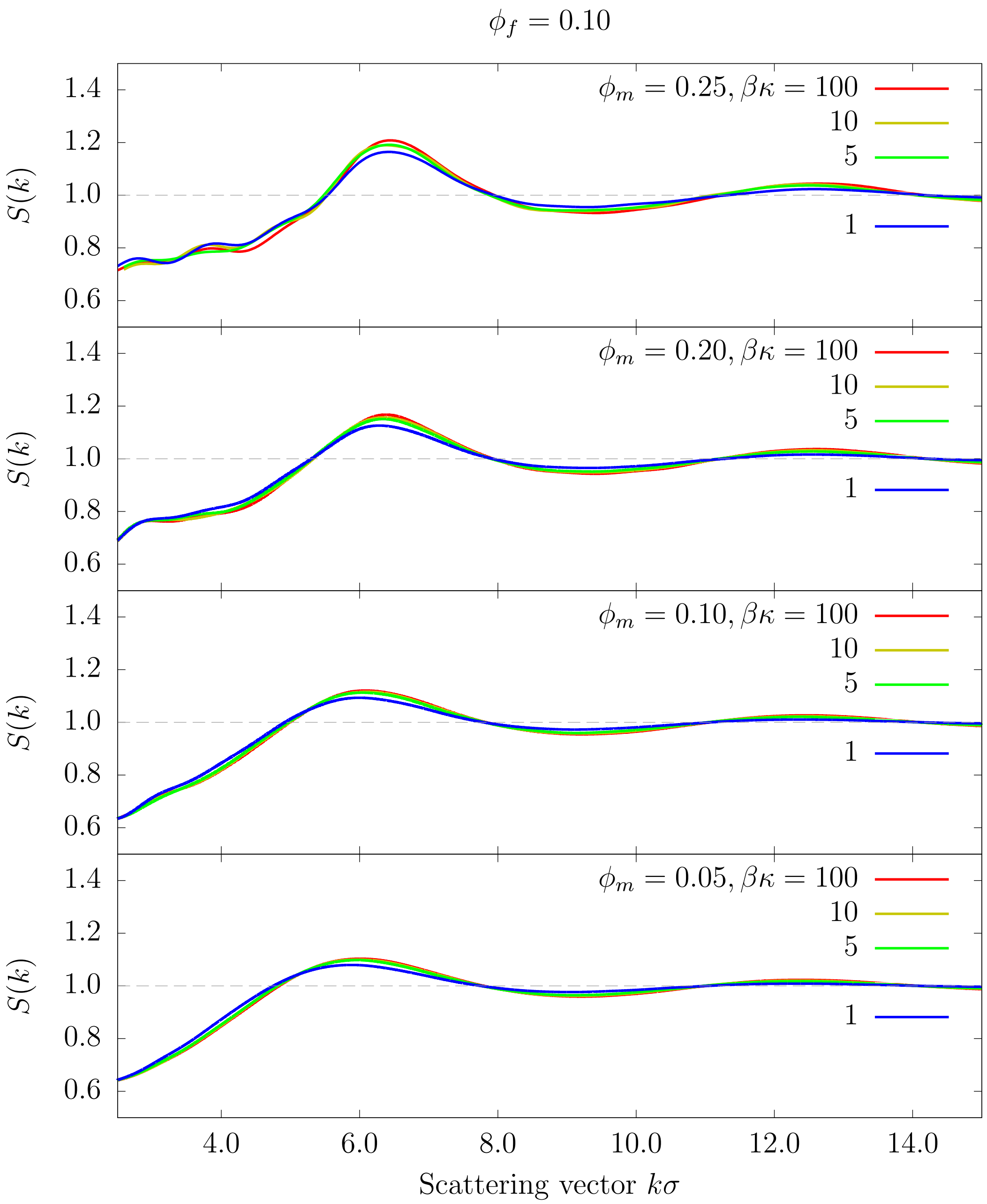

Figure 6.10: Static structure factor $S(k)$ of a DHS-QA-system calculated along path IV with a fluid packing fraction $\phi_f = 0.10$ and various combinations of matrix packing fractions ϕ_m and stiffness parameters $\beta\kappa$ (as labeled) as a function of k in units of σ.

fraction ϕ_f, by focusing on differences in the effect of deformability between the first three paths I-II and path IV.

6.3.1 Deformability and static structure

First we have a look at the static structure factor. In Subsection 6.2.2 we observed that, depending on the position in parameter space, at the regime of glassy states (for the limit of inflexible particles) the first peak of the SSF reaches the Hansen-Verlet threshold.

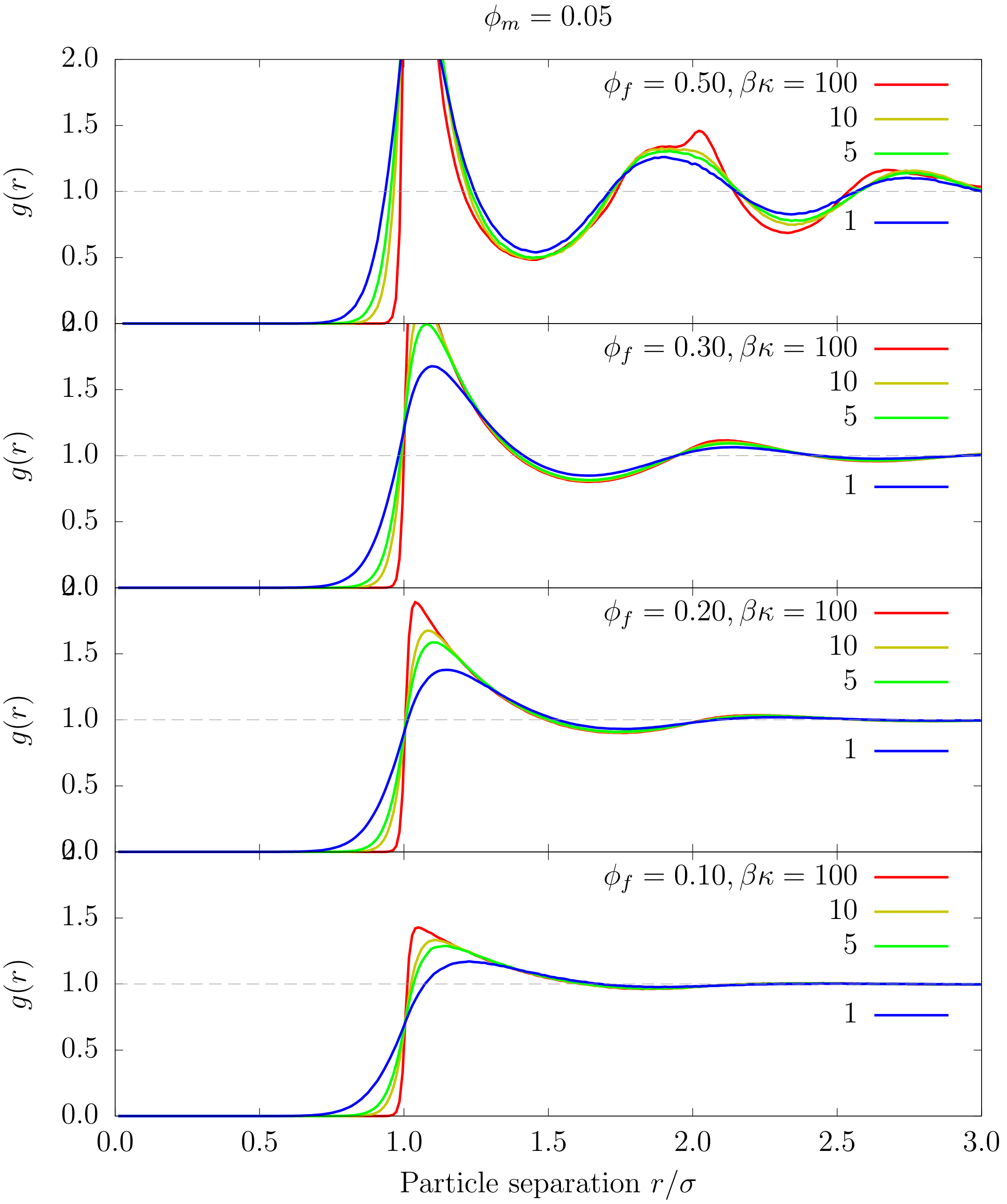

Figure 6.11: Radial distribution $g(r)$ for a DHS-QA-system calculated along path I with a matrix packing fraction $\phi_m = 0.05$ and various combinations of fluid packing fractions ϕ_f and stiffness parameters $\beta\kappa$ (as labeled) as a function of r in units of σ.

This indicates, as already mentioned, transient crystallites. Therefore, we first analyze the behavior of $S(k)$ at state points along path I for different values of stiffness.

This function is shown in Figure 6.9 for $\phi_f = 0.05$ and different values of ϕ_m and $\beta\kappa$. As a reminder, in the Chapters 4 and 5 we found no major impact of deformability on the SSF for systems within the DHS model which do not show a crystalline structure. In this respect path I is ideal to identify an impact of stiffness $\beta\kappa$ on $S(k)$ in combination with an increasing fluid packing fraction ϕ_f, since the matrix packing fraction is fixed at the smallest simulated value of $\phi_m = 0.05$.

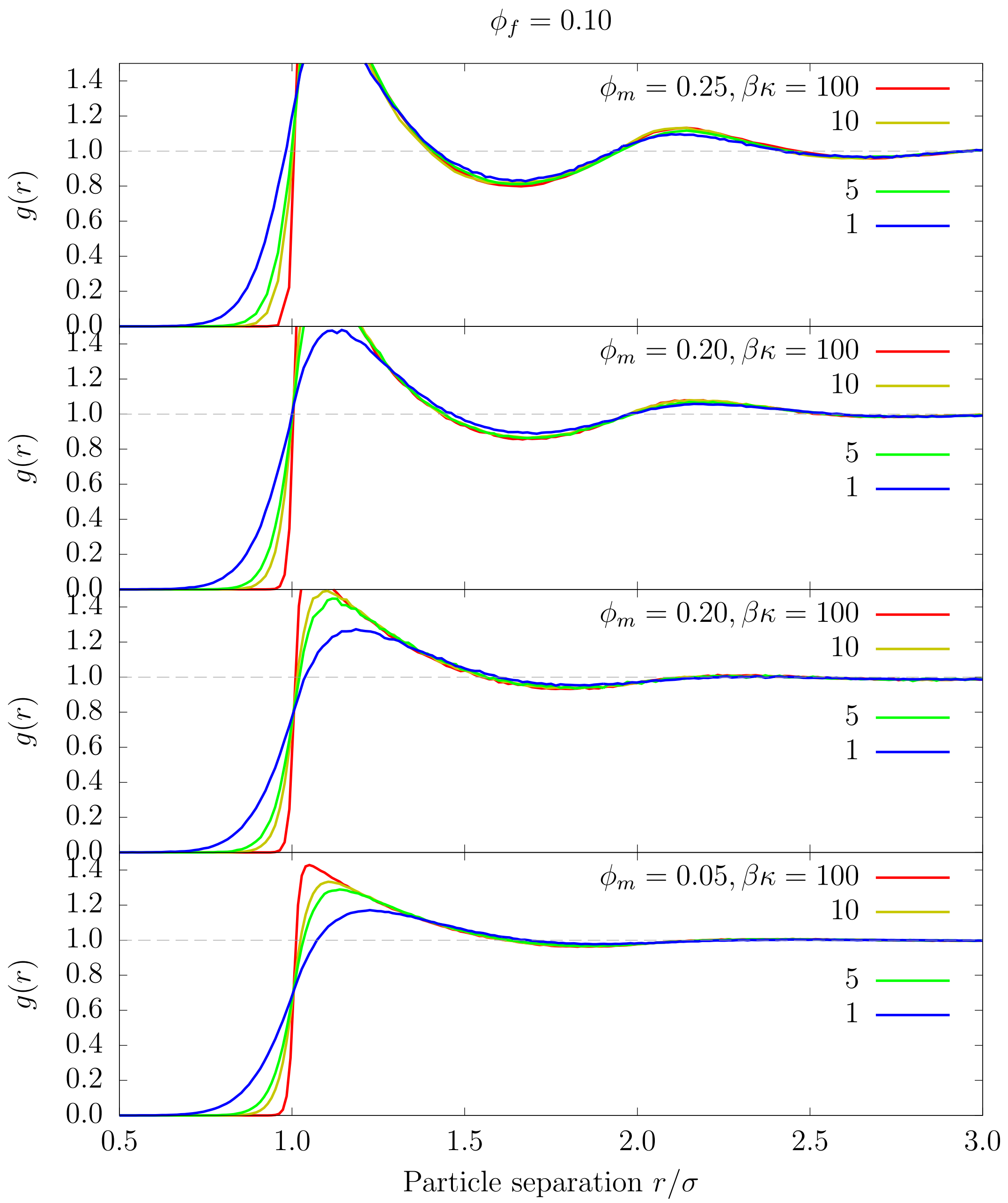

Figure 6.12: Radial distribution $g(r)$ for a DHS-QA-system calculated along path IV with a fluid packing fraction $\phi_f = 0.10$ and various combinations of matrix packing fractions ϕ_m and stiffness parameters $\beta\kappa$ (as labeled) as a function of r in units of σ.

Contrary to the simple DHS-system we find a dependence of the SSF on the deformability of the particles. For stiffness parameters $\beta\kappa \in [100, 10, 5, 1]$ we observe a decreasing height of the first peak of $S(k)$ for decreasing stiffness. For small fluid packing fractions $\phi_f = 0.10$ and 0.20 the change is little, however, we observe an increasing effect when increasing ϕ_f to 0.30 and above. For the highest fluid packing fraction $\phi_f = 0.50$, where we found out in Section 6.2 that this is a state point of the glassy regime, the height of the first peak drops even below the Hansen-Verlet threshold of ~ 3 for $\beta\kappa < 10$ (i.e. strong deformability). This observation can be interpreted that for higher deformability particles tend to form less local crystalline structures. In addition, it can be seen that also all local oscillations in $S(k)$ vanish for the state with the largest value of ϕ_f along path I.

Figure 6.10 depicts $S(k)$ for state points along path IV for stiffness parameters $\beta\kappa \in [100, 10, 5, 1]$. Path IV is ideal to identify for possible effects of deformability in combination with an increasing matrix packing fraction. Similar as in the case of path I, a tendency for a smoothing of the different local maxima in $S(k)$ can be observed for decreasing stiffness $\beta\kappa$, but not as pronounced as along path I. This is most probable to the fact that it gets less probable for fluid particles to meet in systems on path IV, due to additional matrix particles obstructing their movement. Therefore, for all state-points the first peak of the SSF never reaches a value higher than ≈ 1.2 and deformation of particles cannot restrict the already less probable formation of transient crystallites.

As in the previous chapters we want to combine our observations on the static structure factor with the radial distribution function, which shows the same information about the static structure, but with different peculiarities. In section 6.2.2 we saw split-type peaks for $r = 2\sigma$ emerging in the RDF for some state points in the glassy regime, but overall fluid or amorphous structure over the whole phase space.
Further in Chapter 4 we found that under the DHS model the only effect of deformability on the RDF, for state points without a full crystalline structure, is a smoothing of the first peak of $r = \sigma$. This is due to the fact that particles with the ability to deform can approach each other further if their aspect ratio x diverges more from unity (and therefore one of the two lengths a and c of the semi axis reaches below the particle diameter σ).

Under the DHS-QA model the RDF for the same paths I-IV as before are pictured for a range of stiffnesses $\beta\kappa \in [100, 10, 5, 1]$ in the Figures 6.11 and 6.12. For Figure 6.11 on path I we observe similar properties of a smoothed form of the RDF as in the case of the SSF. There are negligible effects of deformability for sparse fluid packing fraction, but they increase drastically for increasing ϕ_f. For $\phi_f = 0.50$ the split-type peak of $r = 2\sigma$ even completely vanishes for slightly more flexible particles of $\beta\kappa = 10$. The overall form of the RDF does not show the typical form of a glassy or amorphous state, but instead resembles a full fluid state.

Additionally, in contrast to the simple DHS model all peaks show increasing shrinkage for increasing fluid packing fraction and deformability. For the first peak we observe the typical progress into the region of $r < \sigma$ similar to findings of Chapter 4. These traits could indicate a shifting of the transition line for the type-B transition shown in Figure 6.2 towards the region of higher ϕ_f under decreasing stiffness.

Figure 6.12 depicts the RDF for path IV with its fixed fluid packing fraction $\phi_f = 0.10$ for increasing matrix packing fraction at various stiffness parameters. In contrast to the previous observations in case of path I we find for all configurations the same slight decrease of the peaks in the RDF, but compared to the effect of deformability combined with increasing fluid packing fraction it is negligible. The most apparent reason is the same we gave for the SSF, that the separation due to matrix particles represses the formation of crystallites, which therefore cannot be relieved through decreasing stiffness.

The last feature of our system that we will analyze, to get a profound understanding of its static structure, is the distribution of aspect ratio (ARD) of the particles. This

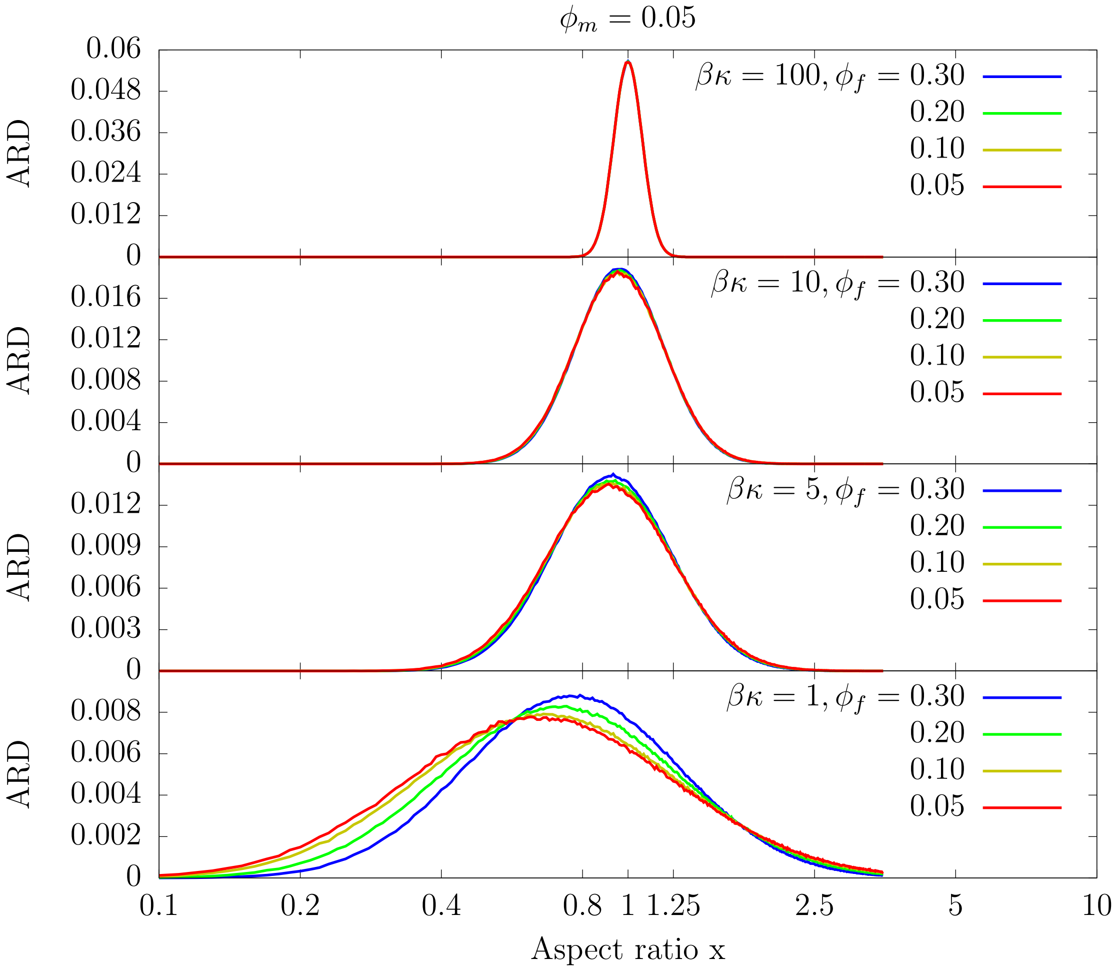

Figure 6.13: Distribution of aspect ratio $ARD(x)$ for a DHS-QA-system calculated along path I with a matrix packing fraction $\phi_m = 0.05$ and various combinations of fluid packing fractions ϕ_m and stiffness parameters $\beta\kappa$ (as labeled) as a function of x.

property gives insight into the deformation of the particles. In Chapter 4 we found out that the general form of the ARD shows the similar features for all values of deformabilty. This quantity is essentially a Gaussian distribution; for decreasing $\beta\kappa$ the maximum value of the distribution tends to move from spherical ($x = 1$) towards oblate ($x < 1$). In addition, the variance of the distribution increases with deformability giving access to more extreme deformations to oblate or prolate particle shapes. For systems without a full crystalline structure a change in the packing fraction has no influence on the shape of the ARD.

Figure 6.13 depicts different ARD's for state points on path I. Like before the range of stiffnesses is in $\beta\kappa \in [100, 10, 5, 1]$. Similar to our observations of Section 4.1 on the ARD we observe the same shapes and the movement of the maximum of the distribution towards the oblate shape ($x < 1$) for decreasing stiffness $\beta\kappa$. In contrast to these previous results, where we analyzed systems with a similar total packing fraction, we observe now a dependence of the ARD on the packing fraction. With increasing ϕ_f the maximum of the distribution is moved back towards the spherical shape ($x = 1$). The probability (area below the distribution) of particles being in oblate shape is decreasing, while the

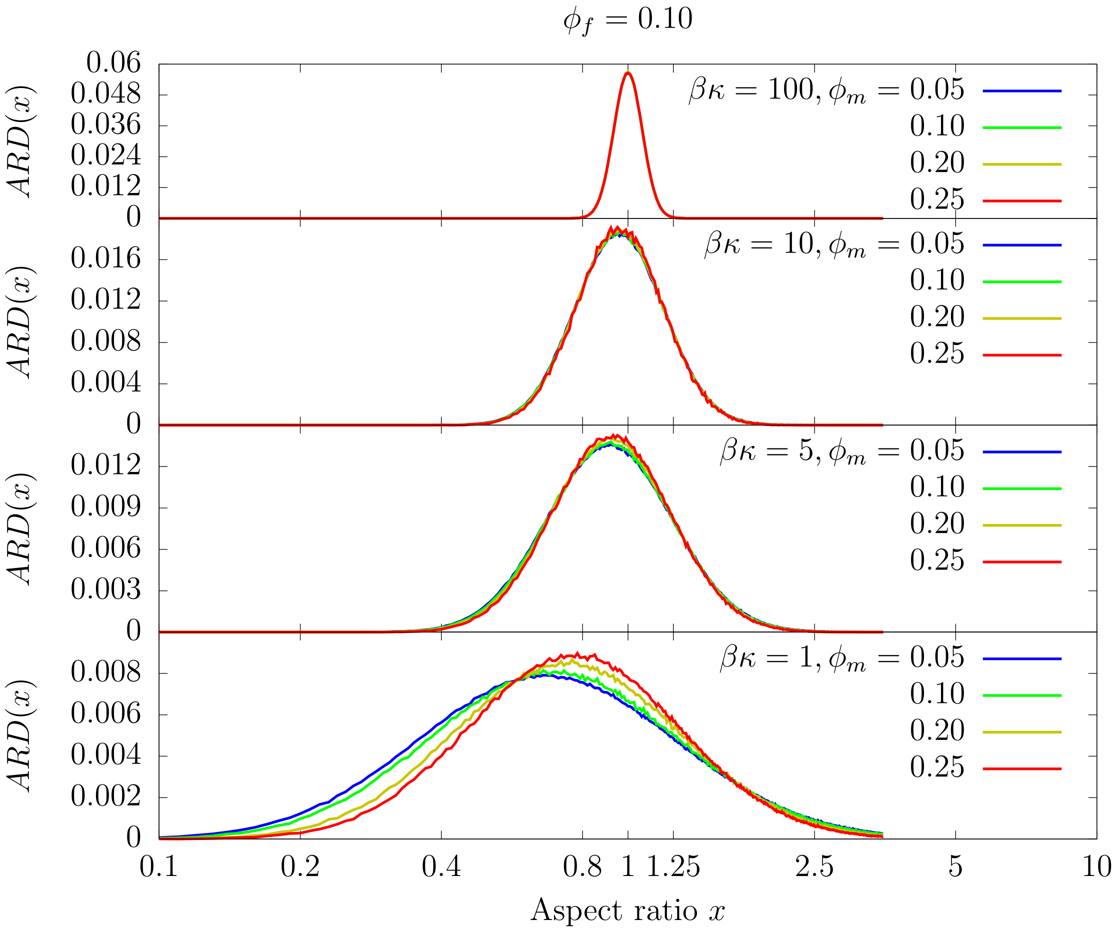

Figure 6.14: Distribution of aspect ratio $ARD(x)$ for a DHS-QA-system calculated along path IV with a fluid packing fraction $\phi_f = 0.10$ and various combinations of matrix packing fractions ϕ_m and stiffness parameters $\beta\kappa$ (as labeled) as a function of x.

probability of particles being in prolate shape is relatively unchanged. This behavior was previously only observed for systems in an ordered state (see Section 5.1).

Figure 6.14 depicts different ARD's for state points on path IV. We observe for increasing matrix packing fraction and constant fluid packing fraction the same obstruction of the oblate shape of the particles as on path I, even though there is only a small fraction of deformable fluid particles on state points of path IV (compared to the DHS-system, where it was only observed for $\phi_{tot} > 0.52$). This indicates that the oblate shape becoming unfavorable for low total packing fractions is solely due to space being blocked by the static matrix particles; i.e. QA-DHS-system cannot adapt as a whole to the increasing packing fraction, like a DHS-system would do.

6.3.2 Deformability and dynamic behavior

The last feature of the DHS-QA model that we have to investigate is the effect of deformability on the dynamics of the particles as compared to the simple HS-QA model.

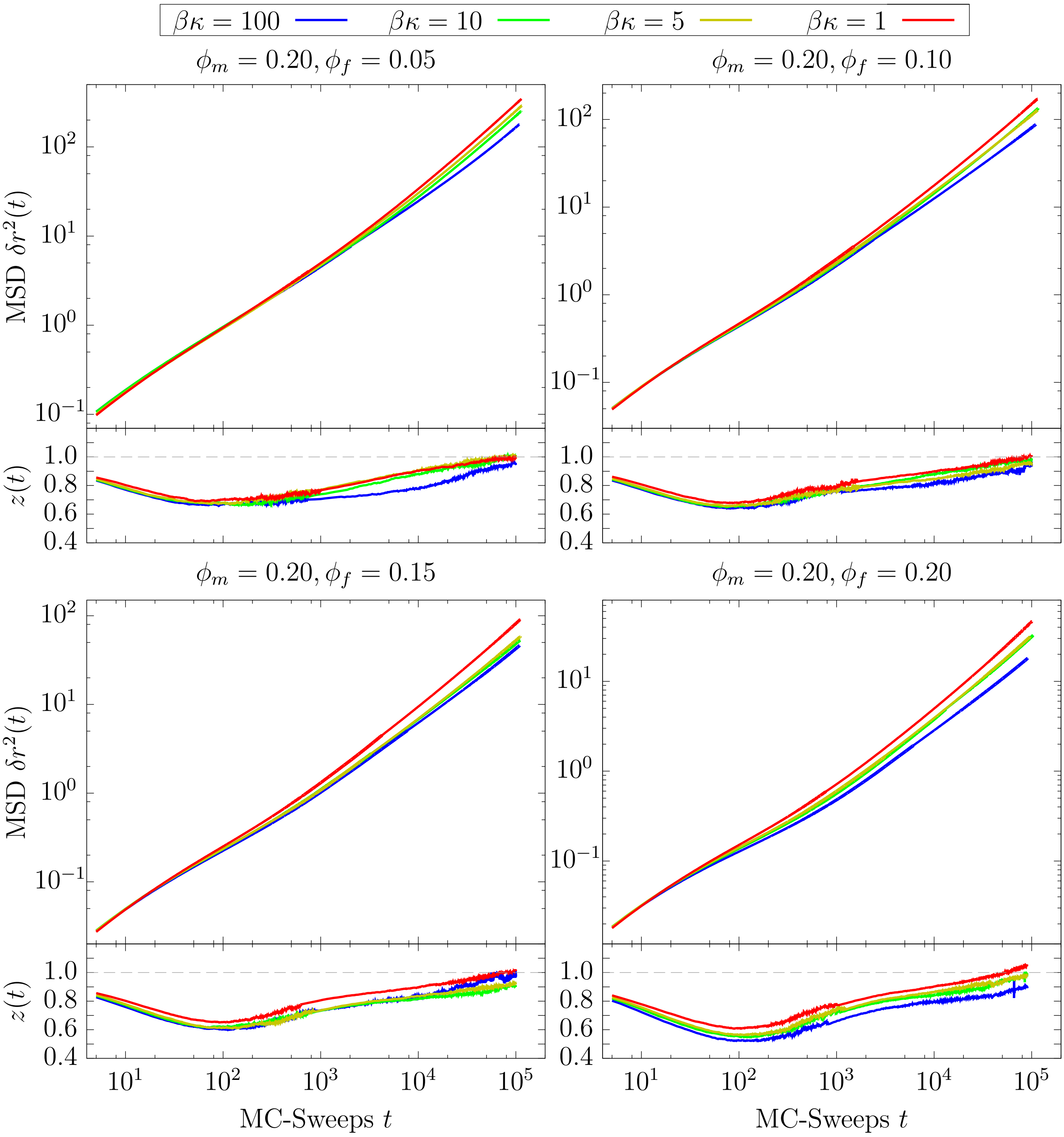

Figure 6.15: Mean squared displacement $\delta r^2(r)$ and its logarithmic derivate $z(t)$ for a DHS-QA-system calculated along path III with a fluid packing fraction $\phi_m = 0.20$ and various combinations of fluid packing fractions ϕ_f and stiffness parameters $\beta\kappa$ (as labeled) as a function of t.

There we observed different types of behaviour of the MSD $\delta r^2(t)$ and its logarithmic derivate $z(t)$. In this subsection we therefore want to take a look at how these properties are affected by the deformations of the particles.

Since we saw that all simulated systems for path I tend to end with a long-range value of $z = 1$ and therefore normal diffusion, we want to focus on path III to look into

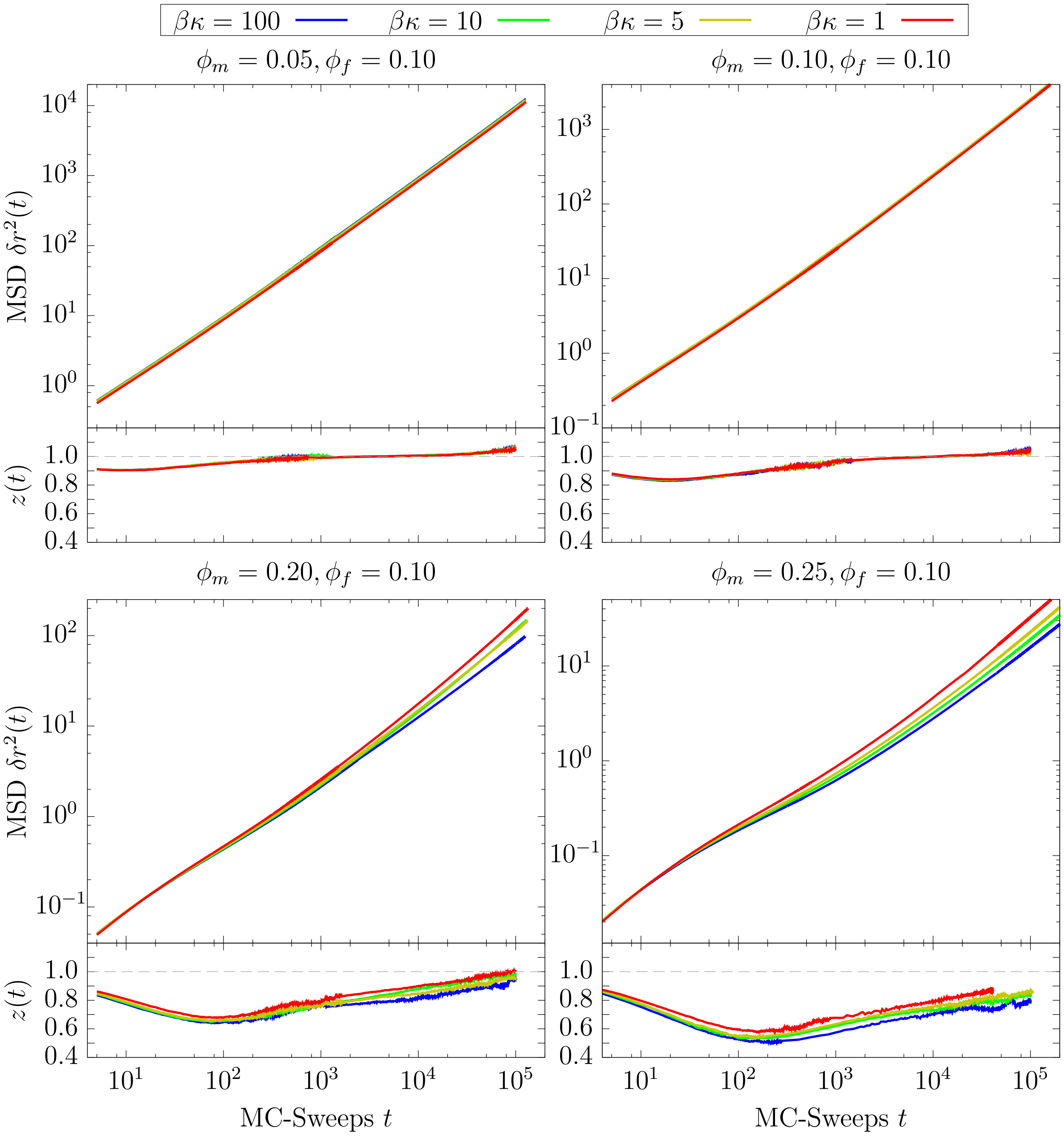

Figure 6.16: Mean squared displacement $\delta r^2(r)$ and its logarithmic derivate $z(t)$ for a DHS-QA-system calculated along path IV with a fluid packing fraction $\phi_f = 0.10$ and various combinations of matrix packing fractions ϕ_m and stiffness parameters $\beta\kappa$ (as labeled) as a function of t.

combined effects of varying deformability and fluid packing fraction. Along path III for the case of undeformable particles (i.e. $\beta\kappa = 100$) we observed a long time sub-diffusive behavior with $\lim_{t\to\infty} z(t) \approx 0.78$. Through analyzing the form of $\delta r^2(t)$ and $z(t)$ along path IV, we observed a similar behavior for higher matrix packing fractions, where the exact long time value of $z(t)$ depends only on the magnitude of ϕ_m. This anomalous diffusion we observed is of high interest for in this subsection, hence we will focus in the following on path III and path IV for the discussion of our results.

Figure 6.15 shows $\delta r^2(t)$ and $z(t)$ for various state points along path III at different values of $\beta\kappa$. From top-left to bottom-right the panels show the MSD together with $z(t)$ for increasing fluid packing fraction ϕ_f and a fixed matrix packing fraction $\phi_m = 0.20$. For all systems we observe clear effects of deformability. For $\delta r^2(t)$ we observe the typical plateau at intermediate times reaching a normal diffusive state for low ϕ_f and a subdiffuive state for higher values of ϕ_f at large time scales. For all state points we observe that for increasing deformability the particles are traveling longer distances (i.e. $\delta r^2(t)$ reaches higher values), which means the particles are less obstructed by their neighbor fluid or matrix particles.

The change in mobility is even better reflected via the logarithmic derivate $z(t)$. Its value decreases over all time scales and values of fluid packing fractions, when increasing deformability. For the highest shown packing fraction $\phi_f = 0.20$ the anomalous diffusion even turns into normal diffusion for the system with lowest stiffness parameter of $\beta\kappa = 1$. These observations can be interpreted such that the particles gain access to paths through the porous matrix, via deforming themselves, while these paths would not be accessible for rigid spherical particles. Via deformation they gain their ability to move larger distances even while being obstructed by matrix particles.
These features of the MSD suggest a further interpretation of the findings from the ARD of Subsection 6.2.2. Particles seem to adapt to the matrix into which they are immersed by changing into specific forms, which seem to be, according to the ARD, a more prolate form.

Lastly we take a look at $\delta r^2(t)$ for varying matrix packing fraction at different deformabilities, where we choose path IV again, because it gives the best access to these effects. Like before this path seems optimal to separate the effects of ϕ_m from ϕ_f. The results are shown in Figure 6.16.
For lower matrix packing fraction we do not find any effect of deformability on the MSD and its derivate z, visible on the two top pictures. But when reaching the regime of localization with $\phi_m = 0.20$, we find again that the particles regain their ability to move less obstructed by the matrix. The meaning of this gets more clear when looking precisely at the change in ϕ_m. Even though there is only a small increase in matrix packing fraction compared to the left bottom picture, the right bottom picture shows big jumps in the long-time value of $z(t)$. This means that even though the number of matrix particles blocking paths of fluid particles or even confining them completely is increasing, do the fluid particles regain an even bigger part of mobility through adapting their form to the matrix. Like this the gain access to paths and the ability to slip through holes in the matrix which would not be possible otherwise.

CHAPTER 7

Conclusion

Finally, this last chapter serves the purpose of summarizing all results presented throughout this thesis and to draw a clear line to connect all these insights. Further we will provide possible ways to carry on the research on the DHS-QA model and what could possibly bring ways of gaining an even deeper understanding of it.

The main goal of this thesis was to give the reader a profound understanding of the deformable-hard-spheroid model (DHS model). This includes the presentation of what changes a system undergoes when its particles gain the ability to deform from the usual spherical form. For this purpose we gave a fundamental overview of theoretical calculation which build the foundation of the DHS model in Chapter 2. Further we introduced simulation techniques used to generate configurations obeying the DHS model in Chapter 3. Additionally, in the same chapter the statistical tools needed to derive and calculate static and dynamic traits from these configurations were presented. We used these tools then to compare the results from already well established and investigated models like HS-models with the ones from the DHS-model.

To get a fundamental understanding of the physics we could draw from the variety of simulations, we separately showed the static structure and dynamic properties of state points in the fluid regime of the DHS-model in Chapter 4 and the ordered regime in Chapter 5. We tried to focus in particular on the changes that occur when moving from the fluid to the ordered state.
Over these two chapters we found the basic augmentation that deformation brings into the DHS-model, compared to other models. Particles in a fluid phase tend to deform randomly, therefore gain no mobility from deforming (Sections 4.1,4.2). But when local or long-range order becomes apparent in a system, deformation shows major effects. Rigid crystalline structures loosen when particles deform and transient crystallites tend to have a shorter lifetime. Furthermore, particles in a system showing signs of complete confinement regain their mobility and break this confinement only showing the traits of short time caging instead (Section 5.2). In addition systems with high packing fractions show correlations of inter-particle-orientation, which indicates another denser solid state, that can be reaches by deformable particles (Section 5.1).

After discussing the DHS model thoroughly, we introduced HS-QA model which was derived and researched by Kurzidim et. al. [7]. We combined this model with the DHS model to gain the DHS-QA model. In the first part of Chapter 6 gave an overview of the HS-QA model by using the limit of nearly rigid particles of the DHS-QA model (Section 6.2). There we observed that even the sparsest matrix completely suppresses the formation of long range order of a system. Therefore, the attainable states are only fluid, localized or glassy states. (Section 5.1) Furthermore in the dynamics of the HS-QA model we observed that many kinds of anomalous subdiffusion can be found for different state points.

Finally, we reached the main achievement of this thesis. We introduced deformability for the particles of the DHS-QA model and could identify the changes it causes in the static structure and dynamics of systems of porous media. We could observe that systems with a glassy structure can revert back to a fluid form (Section 6.3.1) and particles in confinement regain parts of their mobility. We further found that the form the particles assume is dependent on the matrix they move through. This means they adapt and change their form into one necessary for moving through their environment.

Further research on the DHS-QA model could be done, by also calculating the self-intermediate scattering function to gain additional insight on the dynamics and compare them to the HS-QA model. In addition, it would be possible to separate the dynamical properties like the mean-squared-displacement and the ISF into total, self and collective parts. By doing that localization transition and type-A or B transition could be easier identified for the DHS-QA model.
Finally by simulating more systems near the transition lines the exact form of the 3-dimensional phase space which spans the DHS-QA model could be identified. During this thesis we found signs of a shift in the transition lines, but we lacked a proper theoretical calculation method of these to further investigate these findings. But we believe that the DHS-QA model is a good candidate to gain a profound understanding of the physics behind many phenomena occurring e.g. in glassy materials, porous media or the movement of proteins in our cells. It could be a good candidate to build a solid theoretical foundation for these physical events and to gain additional knowledge, therefore for sure is worth of further research and investigation.

List of Figures

Bibliography

[1] D. Richter B. Farago. Shape and size fluctuations of microemulsion droplets: The role of cosurfactant. *Phys. Rev. Lett.*, 65:3348, 1990.

[2] V. M. Batista. *Deformable spherical colloids*. PhD thesis, University of Cambridge, Department of Chemistry, 2011.

[3] L. Van Hove. Correlations in space and time and born approximation scattering in systems of interacting particles. *Physical Review*, 95, 1954.

[4] L. Verlet J. P. Hansen. Phase transitions of the lennard-jones system. *Phys. Rev.*, 184, 1969.

[5] M. S. Wertheim J. W. Perram. Statistical mechanics of hard ellipsoids. 1. overlap algorithm and the contact function. *Journal of Computational Pysics*, 58:409–416, 1985.

[6] V. Krakoviack. Mode-coupling theory predictions for the dynamical transitions of partly pinned fluid systems. *Physical Review E*, 84, 2011.

[7] J. Kurzidim. *Glass Formation of Colloids in Porous Media*. PhD thesis, Technical university of Vienna, Department of theoretical physics, 2013.

[8] V. Sánchez-Gil, E.G. Noya, L. Temleitner, and L. Pusztai. Reverse monte carlo modelling: the two distinct routes of calculating the experimental structure factor. *Journal of molecular liquids*, 207:1–15, 2015.